

Super-resolution and super-sensitivity of quantum LiDAR with multi-photonic state and binary outcome photon counting measurement

Priyanka Sharma¹, Manoj K Mishra², and Devendra Kumar Mishra^{1*}

¹*Department of Physics, Banaras Hindu University,
Varanasi-221005, India*

and

²*Space Applications Centre, Indian Space Research Organization (ISRO), Ahmedabad, Gujarat, India*

(Dated: September 22, 2023)

Here we are investigating the enhancement in phase sensitivity and resolution in Mach Zehnder interferometer (MZI) based quantum LiDAR. We are using multi-photonic state (MPS), superposition of four coherent states [1], as the input state and binary outcome parity photon counting measurement and binary outcome zero-nonzero photon counting measurement as the measurement schemes. We thoroughly investigate the results in lossless as well as in lossy cases. We found enhancement in resolution and phase sensitivity in comparison to the coherent state and even coherent superposition state (ECSS) based quantum LiDAR. Our analysis shows that MPS may be an alternative nonclassical resource in the field of quantum imaging and quantum sensing technologies, like in quantum LiDAR.

I. INTRODUCTION

Radar and its optical counterpart, light detection and ranging (LiDAR), are well-established and broadly used technologies. The first is typically exploited for long-range detection, while LiDAR, operating at visible to near-infrared wavelengths, offers improved resolution yet at a shorter distance. LiDAR (laser radar), a combination of laser technology and modern photoelectric detection technology, has advantages over traditional radar such as high resolution, strong anti-interference ability, and good low-altitude detection performance. However, with continuous application in aerospace, military, artificial intelligence and other fields, LiDAR has reached the limits of classical physics and cannot meet the requirements in detection, measurement, and imaging. Several industries, such as automotive, robotics, unmanned aerial vehicles, etc., heavily rely on LiDAR [2].

With the emergence of quantum metrology [3], the quantum version of LiDAR has been proposed to achieve better precision and resolution [4]. Quantum metrology exploits non-classical resources [5], like entanglement [6] and squeezing, to measure a physical parameter with enhanced resolution and precision than any strategy with classical resources [7]. Examples of different quantum metrology [8] protocols are quantum illumination (QI), quantum-enhanced position and velocity estimation, quantum phase estimation [9–11], transmission parameter estimation, noise estimation and estimation of separation between objects among others. These protocols retrieve the information about an object by interrogating it with a signal beam and the scheme can be seen as an interferometric setup where a channel depending on the parameter of interest is applied to the signal mode.

In a quantum LiDAR system, resolution and sensitivity are the important parameters to determine the range

and image of a target [4, 12]. A standard MZI with the coherent state $(|\alpha\rangle = e^{-|\alpha|^2} \sum_{l=0}^{\infty} (\alpha^l / \sqrt{l!}) |l\rangle)$, where $|\alpha\rangle$ is coherent amplitude and $|l\rangle$, is the Fock state) as one of the inputs results the intensity measurement at one of the output ports either $I \propto \sin^2(\phi/2)$ or $\cos^2(\phi/2)$, ϕ being the phase experienced by the interferometer. This shows the oscillatory pattern with the resolution determined by the ‘full width at half maximum’ (FWHM) of the intensity signal and the wavelength λ . Since, $\text{FWHM} = \pi$ for the $\sin^2(\phi/2)$ or $\cos^2(\phi/2)$ and, hence, fringe resolution can be written as $\Delta x \propto \text{FWHM} \times \lambda/2\pi = \lambda/2$. This is termed as the Rayleigh resolution limit [6, 13]. Beating the Rayleigh limit is termed as the super-resolution and one can achieve this by using the coherent state with quantum detection scheme [14], entangled photons [15, 16], post-processing technique [17], post-selection technique [15, 18], etc. Next to the resolution of the interferometer, phase sensitivity measurement has its own quantum limit termed as shot-noise limit (SNL), $\Delta\phi_{\text{SNL}} = \frac{1}{\sqrt{\bar{n}}}$, where \bar{n} is the mean photon number. One can attain this limit by using a coherent state along with vacuum as the input of the interferometer. Beating the SNL qualifies the measurement for being super-sensitive [19, 20]. We can beat the Rayleigh limit and SNL by utilizing non-classical resources [6, 21–26].

Non-classical state such as N00N state [6] (an equal coherent superposition of N photons) is a prominent example by which one can beat the SNL and saturate the Heisenberg limit (HL), i.e., $1/\bar{n}$. However, in the presence of loss and noise, the N00N states are highly fragile making it difficult to achieve the super-phase sensitivity and super-resolution [27, 28].

To surpass the conventional Rayleigh limit, Gao *et al.* [14] presented a super-resolving quantum LiDAR method with coherent states (CS) and photon-number-resolving detectors. Coherent state as one of the inputs of MZI, Distante *et al.* [17] established the super-resolution with $x \propto \lambda/2N$. Small noise, however, significantly reduced

* Corresponding author: kndmishra@gmail.com

the possible phase sensitivity and the fringe resolution [29]. Wang *et al.* [30] used even coherent superposition state (ECSS) to get two-fold super-resolution compared to CS in lossless and noiseless cases.

Superposition of optical coherent states act as qubits (quantum states defined in a two-dimensional Hilbert space) and have many applications in quantum technology like quantum computation, teleportation, key distribution, etc. Passage of such superposition of coherent states from a 50:50 beam splitter can be used to generate entangled coherent states [31]. Ququats and qutrits defined in four and three-dimensional Hilbert space, respectively, have attracted much attention as they offer an advantage in secure quantum communication [32–35]. Ququats and qutrit are a carrier of quantum information realized by a four- and three-level quantum system in analogous with the terms “qubit” and “qudit” meaning such carriers of quantum information that are realized, correspondingly, by two-level and d-level quantum systems.

In this paper, we are considering four multi-photonic state (MPS) with $(4n + j)$, ($j = 0, 1, 2$ or 3 , and $n = 0, 1, \dots, \infty$), numbers of photon as proposed by Mishra *et al.* [1] to investigate the possibility of super-sensitivity and super-resolution of quantum LiDAR. Superposition of coherent states can be used to encode ququat using these MPS as basis vectors of a four-dimensional Hilbert space. These MPS injected to a 50:50 beam splitter result in bipartite four-component entangled coherent states, i.e., the entangled ququats. MPS [1] is defined as

$$|\psi_j\rangle = N_j \sum_{m=0}^3 (-i)^{jm} |(i)^m \alpha\rangle, \quad (1)$$

where N_j ($j = 0, 1, 2, 3$) is the corresponding normalization constant of the state. Different nonclassical properties of MPS applicable in quantum technology have been studied and an experimental scheme for the generation of MPS has been proposed [1].

The paper is organized as follows. In section II, we discuss MPS and its Wigner function. In Section III, we discuss the MZI as quantum LiDAR in which we describe the basic working of MZI, parameter estimation, and detection schemes. Section IV contains the observation with MPS and vacuum state as the inputs of the MZI and Section V describes the observation with MPS and coherent state as the inputs of the MZI. In Section VI, we conclude our results.

II. MPS AND ITS WIGNER FUNCTION

A. MPS

In this section, we are discussing our state of interest. We chose six different states for the calculation of the resolution and phase sensitivity. These six states are de-

rived from the Eq. (1) and for calculation simplicity, these states combinedly written as [1]

$$|\psi_j\rangle = N_j (A|\alpha\rangle + B|\beta\rangle + C|\gamma\rangle + D|\delta\rangle), \quad (2)$$

where $j = 0, 1, 2, 3$ and $|\beta\rangle = |i\alpha\rangle$, $|\gamma\rangle = |- \alpha\rangle$ and $|\delta\rangle = |- i\alpha\rangle$. All four coefficients are defined as

$$A = 1, B = (-i)^j, C = (-i)^{2j}, D = (-i)^{3j}. \quad (3)$$

The normalization constant of the combined state N_j is written as

$$|N_j| = \left(X + 2Ye^{-|\alpha|^2} \cos(j\pi) + 2Ve^{-|\alpha|^2} \cos\left(|\alpha|^2 - j\frac{\pi}{2}\right) \right)^{\frac{1}{2}}, \quad (4)$$

where,

$$X = (|A|^2 + |B|^2 + |C|^2 + |D|^2), \quad Y = (|A||C| + |B||D|) \\ V = (|A| + |C|)(|B| + |D|). \quad (5)$$

We write our six states by considering proper values of A , B , C , D , and j . For

- (i) CS : $|A| = 1, |B| = |C| = |D| = 0, j = 0$,
we get, $|\alpha\rangle$;
- (ii) ECSS : $|A| = 0, |B| = 1, |C| = 0, |D| = 1, j = 0$,
we get, $(|i\alpha\rangle + |-i\alpha\rangle)$;
- (iii) MPS_{j=0} : $|A| = |B| = |C| = |D| = 1, j = 0$, we get,
 $(|\alpha\rangle + |i\alpha\rangle + |- \alpha\rangle + |-i\alpha\rangle)$;
- (iv) MPS_{j=1} : $|A| = |B| = |C| = |D| = 1, j = 1$, we get,
 $(|\alpha\rangle - i|i\alpha\rangle - |- \alpha\rangle + i|-i\alpha\rangle)$;
- (v) MPS_{j=2} : $|A| = |B| = |C| = |D| = 1, j = 2$, we get,
 $(|\alpha\rangle - |i\alpha\rangle + |- \alpha\rangle - |-i\alpha\rangle)$;
- (vi) MPS_{j=3} : $|A| = |B| = |C| = |D| = 1, j = 3$, we get,
 $(|\alpha\rangle + i|i\alpha\rangle - |- \alpha\rangle - i|-i\alpha\rangle)$.

From Eq. (4), by putting the appropriate values of the variables we can write the normalization constant of the states.

In the context of our subsequent analysis, when we compare certain results across different states, it becomes imperative to standardize the input energy of the interferometer. To achieve this, we must understand how the mean photon number ($N = \langle \hat{a}^\dagger \hat{a} \rangle$) varies with the $|\alpha|^2$ for all six states. In order to do this, we plot the N versus $|\alpha|^2$ graph as shown in Fig. 1. Where,

$$N = N_j \left(X|\alpha|^2 - 2|\alpha|^2 Y e^{-2|\alpha|^2} \cos(j\pi) + 2|\alpha|^2 V e^{-|\alpha|^2} \cos\left(|\alpha|^2 - \frac{j\pi}{2} + \frac{\pi}{2}\right) \right) \quad (6)$$

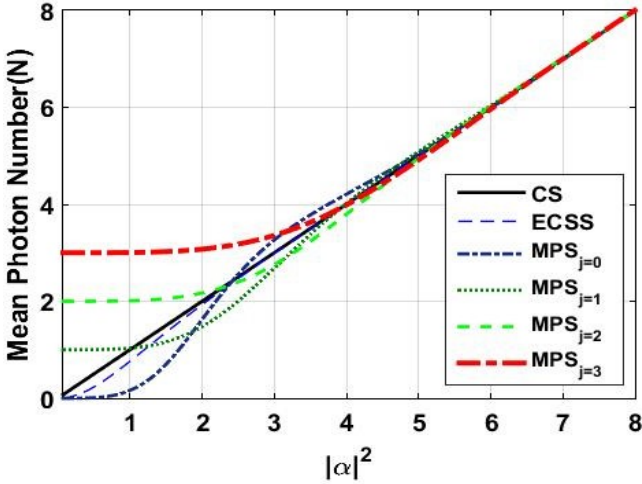


FIG. 1. The plot shows the variation of mean photon number (N) vs. $|\alpha|^2$. Here, we see that for lower values of $|\alpha|^2$, different states possess different mean photon numbers, while for larger values of $|\alpha|^2 (\geq 5)$ they are the same. Note that, for the very small value of $|\alpha|^2 (<< 1)$, some states possess 1, 2 and 3 mean photon numbers and in the figure, it seems for $|\alpha|^2 = 0$.

B. Wigner function of MPS

Wigner function [36, 37] is a phase-space distribution function for a quantum system. The Wigner function has

$$W_j(\lambda) = \frac{2N_j}{\pi} \left(e^s (|A|^2 e^{4p_1} + |B|^2 e^{4q_1} + |C|^2 e^{-4p_1} + |D|^2 e^{-4q_1}) + 2e^{(u+v)} (|A||B| \cos(u+u') + |A||D| \cos(-u+u') + 2e^{-2|\lambda|^2} (|A||C| \cos(4q_1 - j\pi) + |B||D| \cos(4p_1 - j\pi)) + 2|C||D| e^{(u-4p_1+v)} \cos(u-4p_1-u') + 2|B||C| e^{(-u+v)} \cos(u+u') \right), \quad (10)$$

with,

$$\begin{aligned} u &= 2(p_1 - q_1), \quad v = -2|\lambda|^2 - |\alpha|^2, \quad u' = |\alpha|^2 + \frac{j\pi}{2}, \\ \alpha &= x_1 + ix_2, \quad \lambda = y_1 + iy_2, \quad p_1 = x_1 y_1 + x_2 y_2, \\ q_1 &= x_1 y_2 - x_2 y_1, \quad s = -2(|\alpha|^2 + |\lambda|^2). \end{aligned} \quad (11)$$

Where x_1 , y_1 and x_2 , y_2 are the real and imaginary part of the α , λ , respectively.

Eq. (10) is a generalised Wigner function for all six states. Since, from section II A, we know that MPS is a generalised state and by putting appropriate values of the variables (A , B , C , D and j) we write all the six states. So, here, from Eq. (10) we can write the Wigner function for all the six states. Now, we plot the Wigner function for all the states and investigate the nonclassicality for them. To visualize the instances of negativity

turned out to be remarkably useful to characterize and visualize the nonclassicality of a quantum state. The value of the Wigner function lies between -1 and 1 , i.e., $-1 \leq W \leq 1$. For a non-classical state, the Wigner function is always < 0 .

The Wigner function of a state with density operator $\hat{\rho}$, can be defined as

$$W(\lambda) = \frac{1}{\pi^2} \int d^2\eta \text{Tr}[\hat{\rho} \hat{D}(\eta)] e^{-(\eta\lambda^* - \eta^*\lambda)}. \quad (7)$$

Where λ and η are the complex variables and $\hat{D}(\eta)$ is the displacement operator. The density operator for a pure state, $|\psi\rangle$, can be written as $\hat{\rho} = |\psi\rangle\langle\psi|$. Since, the displacement operator is defined as $\hat{D}(\eta) = \exp(\eta\hat{a}^\dagger - \eta^*\hat{a})$, therefore,

$$\text{Tr}[\hat{\rho} \hat{D}(\eta)] = \langle \exp(\eta\hat{a}^\dagger - \eta^*\hat{a}) \rangle. \quad (8)$$

Since the Wigner function follows the normalization conditions, we can write it as

$$\int W(\lambda) d^2\lambda = \int d^2\eta \text{Tr}[\hat{\rho} \hat{D}(\eta)] \delta^{(2)}(\eta) = \text{Tr}[\hat{\rho}] = 1. \quad (9)$$

Therefore, in order to find whether MPS is a classical or nonclassical state we write down the Wigner function of the MPS (given in Eq. (2)). From Eq. (7), Wigner for the MPS is

of the Wigner function, given in Eq. (10), we consider, $x_1 = x_2 = 1$ and plot the Wigner function for all six states with respect to y_1 and y_2 , as shown in Fig. 2. From Fig. 2, we can see that for CS, the Wigner function always gives ≥ 0 . Which shows that CS is a classical state. On the other hand, the Wigner function of the other five states (ECSS, $\text{MPS}_{j=0}$, $\text{MPS}_{j=1}$, $\text{MPS}_{j=2}$ and $\text{MPS}_{j=3}$) showing negative values. Here, $\text{MPS}_{j=1}$ and $\text{MPS}_{j=3}$ shows high negativity in comparison to the other states. Hence, the negativity of the Wigner function provides the signature of nonclassicality of $\text{MPS}_{j=0,1,2,3}$.

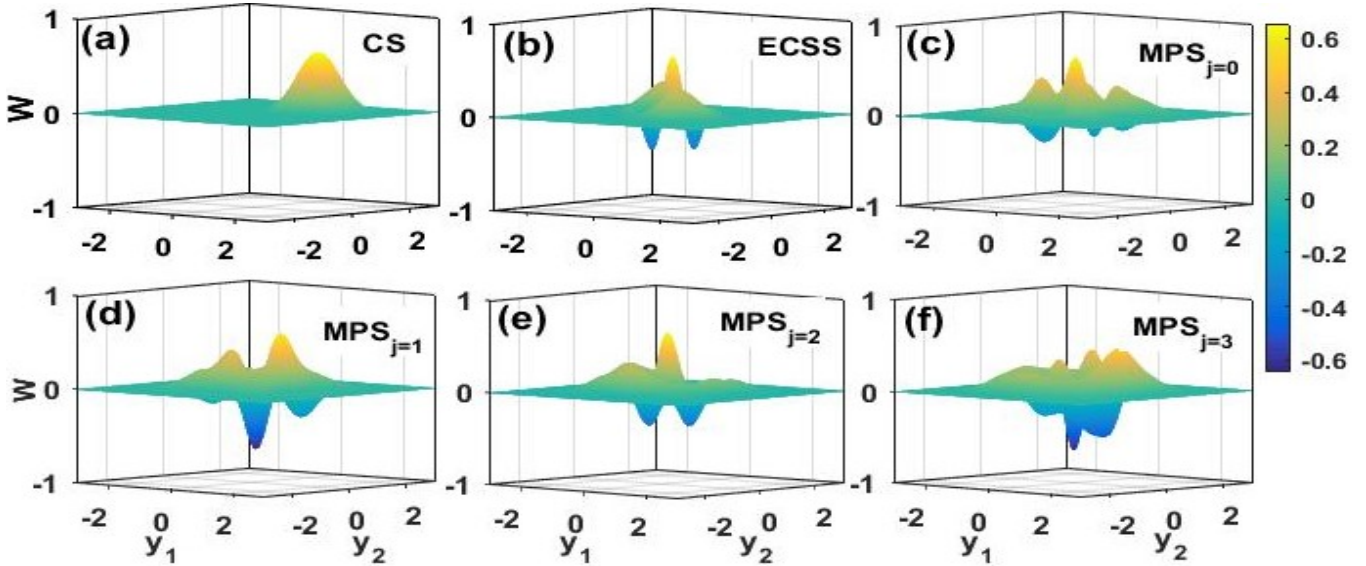
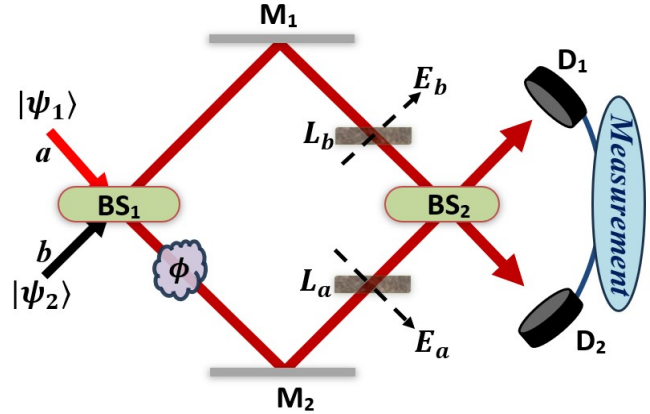


FIG. 2. Plots show the Wigner function distribution for all six states. The colour bar shows the corresponding values of the Wigner function. The negative values show the condition on y_1 and y_2 for a state to become a nonclassical state. Here, we consider $x_1 = x_2 = 1$.

III. MACH-ZEHNDER INTERFEROMETER (MZI) AS A QUANTUM LIDAR

A. Basic working of MZI



The MZI is widely used in quantum sensing and imaging techniques and, here, we consider MZI as a Quantum LiDAR [4]. A schematic block diagram of MZI is shown in Fig. 3.

Working of a typical MZI setup can be understood in three steps: probe preparation, probe evolution, and measurement. In probe preparation, two input beams are combined by BS_1 . Outputs of BS_1 produce reference beam and probe beam. We keep the reference beam for our reference and the probe beam evolves inside the interferometer. In the case of quantum LiDAR, this evolution contains information about the distant object. After the evolution, the probe and reference beams are recombined via BS_2 . In the last step, we carry out the measurement on the output of the BS_2 .

FIG. 3. MZI has two input (modes a , b) and two output ports including two 50:50 beam splitters (BS_1 and BS_2), two mirrors (M_1 and M_2), a phase shifter ϕ , two detectors (D_1 & D_2). The two fictitious beam splitters (L_a and L_b) whose corresponding modes are E_a and E_b , respectively, mimic the photon loss inside the two arms of MZI.

Initially, we consider the states of the system as

$$|\psi\rangle_{in} = |\psi_1\rangle_a \otimes |\psi_2\rangle_b \otimes |0\rangle_{E_a} \otimes |0\rangle_{E_b} \quad (12)$$

Here, $|\psi_1\rangle$ and $|\psi_2\rangle$ are the inputs of the MZI at modes a and b , and modes E_a and E_b are associated with the photon loss (as shown in Fig. 3). When the signals pass through a beam splitter that follows the SU(2) algebra, the input-output relation can be written as

$$\begin{pmatrix} \hat{a}_{out} \\ \hat{b}_{out} \end{pmatrix} = \hat{B} \begin{pmatrix} \hat{b}_{in} \\ \hat{a}_{in} \end{pmatrix}, \quad (13)$$

where \hat{a}_{in} , \hat{b}_{in} (\hat{a}_{out} , \hat{b}_{out}) are the input (output) annihilation operators of the beam splitter. The transformation

matrix of the beam splitter is defined as $\hat{B} = \begin{pmatrix} i\sigma & \tau \\ \tau & i\sigma \end{pmatrix}$, where σ and τ are the reflectance and transmittance of the beam splitter and follow the relation $\sigma^2 + \tau^2 = 1$. For a 50:50 beam splitter, $\sigma = \tau = 1/\sqrt{2}$, the phase change being $\pi/2$ (0) in reflection (transmission).

The phase shift ϕ experienced in the path of the interferometer can be expressed in terms of the unitary evolution operator $\hat{U}(\phi) = e^{i\phi\hat{a}^\dagger\hat{a}}$ with $\phi = 2kf$, where f is the target distance and $k = \frac{2\pi}{\lambda}$ the wave number (λ is the wavelength of the light).

During the evolution process, the probe signal interacts with the environment which causes photon loss in the signal. This photon loss occurs mainly because of scattering and reflection of signals from the different types of objects present in the path. So, in order to consider the photon loss inside the LiDAR, we consider two fictitious beam splitters (L_a and L_b) in each arm mimicking the photon loss have transmittivity t and reflectivity r [38, 39] as shown in Fig. 3.

Here, the transformation matrices associated with 50:50 beam splitters BS_1 and BS_2 are \hat{B}_1 and \hat{B}_2 , respectively, such that $\hat{B}_1 = \hat{B}_2 = \frac{1}{\sqrt{2}} \begin{pmatrix} i & 1 \\ 1 & i \end{pmatrix}$. The transformation matrices associated with fictitious beam splitters L_a and L_b are \hat{B}_{l_a} and \hat{B}_{l_b} such that $\hat{B}_{l_a} = \hat{B}_{l_b} = \begin{pmatrix} ir & t \\ t & ir \end{pmatrix}$. Also, $\hat{U}(\phi) = \begin{pmatrix} e^{i\phi} & 0 \\ 0 & 1 \end{pmatrix}$. With these definitions, we can write the output state as

$$|\psi\rangle_{out} = \left| \psi_{1_{out}}, \psi_{2_{out}}, \frac{ir(\hat{a} + i\hat{b})e^{i\phi}}{\sqrt{2}}, \frac{ir(\hat{b} + i\hat{a})}{\sqrt{2}} \right\rangle_{a,b,E_a,E_b}, \quad (14)$$

where, $\psi_{1_{out}} = \frac{1}{\sqrt{2}} \left(\frac{t(\hat{a} + i\hat{b})e^{i\phi}}{\sqrt{2}} + \frac{it(\hat{b} + i\hat{a})}{\sqrt{2}} \right)$ and $\psi_{2_{out}} = \frac{1}{\sqrt{2}} \left(\frac{it(\hat{a} + i\hat{b})e^{i\phi}}{\sqrt{2}} + \frac{t(\hat{b} + i\hat{a})}{\sqrt{2}} \right)$.

B. Parameter estimation and phase super-sensitivity

In order to perform the measurement on the output of the interferometer, we must have an observable (operator) corresponding to the detection scheme. Let us consider \hat{X} as an operator that contains the information of the unknown phase ϕ to be estimated. The expectation value of this observable with respect to the final state of the system can be written as $\langle \hat{X}(\phi) \rangle = \langle \Psi | \hat{X}(\phi) | \Psi \rangle$. Where $|\Psi\rangle$ is the final state of the system.

A small change of $\delta\phi$ in ϕ rises a change in \hat{X} which can be written as

$$\langle \hat{X}(\phi + \delta\phi) \rangle \approx \langle \hat{X}(\phi) \rangle + \frac{\partial \langle \hat{X}(\phi) \rangle}{\partial \phi} \delta\phi. \quad (15)$$

The difference $\langle \hat{X}(\phi + \delta\phi) \rangle - \langle \hat{X}(\phi) \rangle$ is detected in the experiment only if

$$\langle \hat{X}(\phi + \delta\phi) \rangle - \langle \hat{X}(\phi) \rangle \geq \Delta \hat{X}(\phi), \quad (16)$$

where, $\Delta \hat{X}(\phi) = \sqrt{\langle \hat{X}^2 \rangle - \langle \hat{X} \rangle^2}$ is the standard deviation of $\hat{X}(\phi)$. The value of $\delta\phi$ for which inequality given in Eq. (16) saturates is called the phase sensitivity $\Delta\phi$ and, according to the error-propagation formula, can be written as [23, 40]

$$\Delta\phi = \frac{\Delta \hat{X}}{\left| \frac{\partial \langle \hat{X}(\phi) \rangle}{\partial \phi} \right|}. \quad (17)$$

This equation will be vital in the following sections for the sensitivity of the MZI.

C. Detection schemes

1. Binary outcome parity photon counting measurement (parity detection)

The operator for the parity measurement is described by $\hat{\Pi} = (-1)^\hat{n} = e^{i\pi\hat{n}}$, where $\hat{n} = \hat{a}^\dagger\hat{a}$ is the number operator [41–44]. So, on the basis of photon counts on the output port, we have $\hat{\Pi} = +1$ or $\hat{\Pi} = -1$ for an even number of photons or an odd number of photons, respectively. Its expectation value is obtained by averaging the many measurement repetitions, i.e.,

$$\langle \hat{\Pi} \rangle = \sum_{n=0}^{\infty} (-1)^n P_n \quad (18)$$

where P_n is the probability for n photons in the output state.

In principle, photon counting measurement is expressed by a set of projection operators $\{|k, l\rangle\langle k, l|\}$ with the two-mode Fock states $|k, l\rangle = |k\rangle_a \otimes |l\rangle_b$, where k and l are the photon numbers in the mode a and mode b , respectively. So, the probability of detecting n photons at the output port a and m photons at the output port b is given by

$$P(n, m) = \langle n, m | \hat{\rho}_{out} | n, m \rangle, \quad (19)$$

where $\hat{\rho}_{out} = |\psi\rangle_{out} \langle \psi|$ is the density operator of the output state and $|\psi\rangle_{out}$ is output state of the system. In order to find the probability of getting n photon number at port a , we sum over m . Therefore, Eq. (19) is written as

$$P(n) = \sum_m P(n, m). \quad (20)$$

If the probability of getting an even number of photons, is $P(+)$ and the odd number of photons is $P(-)$ with $P(+) + P(-) = 1$, then the expectation value of parity

operator in terms of even and odd probabilities can be written as

$$\langle \hat{\Pi} \rangle = P(+) - P(-). \quad (21)$$

Using the error propagation formula as written in Eq. (17), phase sensitivity with the parity measurement can be written as

$$\Delta\phi_{\Pi} = \frac{\sqrt{1 - \langle \hat{\Pi} \rangle^2}}{\left| \frac{\partial \langle \hat{\Pi} \rangle}{\partial \phi} \right|}. \quad (22)$$

Here, $\left| \frac{\partial \langle \hat{\Pi} \rangle}{\partial \phi} \right|$ is the variation in $\langle \hat{\Pi} \rangle$ with phase ϕ and we used the property $\hat{\Pi}^2 = 1$.

2. Binary outcome zero non-zero photon counting measurement (Z-detection)

In this measurement scheme, we explore the data obtained by a standard single-photon detector at the output port a that cannot differentiate between different photon numbers [45]. It is also termed as no photon measurement [46]. It has only two outcomes, no photon ($n = 0$) and any number of photons ($n \neq 0$) with the associated probabilities

$$P(0) = \sum_m P(n=0, m), \quad (23)$$

and $P(n \neq 0) = 1 - P(0)$, respectively. For a better approximation, we can take the difference between these two probabilities, i.e., $P(0) - P(n \neq 0)$ [47]. This gives us $P(0) - P(n \neq 0) = 2P(0) - 1$, so considering only $P(0)$ is much simpler to evaluate. Therefore, the observable for zero photon detection is the zero photon projection $\hat{Z} = |0\rangle_a \langle 0|$ and its expectation value will be

$$\langle \hat{Z} \rangle = P(0). \quad (24)$$

So, in order to find the phase sensitivity by using this observable we use the error propagation formula written in Eq. (17). The phase sensitivity in the case of Z-detection can be written as,

$$\Delta\phi_Z = \frac{\sqrt{\langle \hat{Z} \rangle - \langle \hat{Z} \rangle^2}}{\left| \frac{\partial \langle \hat{Z} \rangle}{\partial \phi} \right|}. \quad (25)$$

Here, $\left| \frac{\partial \langle \hat{Z} \rangle}{\partial \phi} \right|$ is the variation in $\langle \hat{Z} \rangle$ with phase ϕ and we have used the property $\hat{Z}^2 = \hat{Z}$.

We will use these two detection schemes for the super-resolution and super-sensitivity of quantum LiDAR.

IV. SUPER-RESOLUTION AND SUPER-SENSITIVITY WITH MPS AND VACUUM STATE AS INPUTS

Here, we are discussing the resolution and phase sensitivity of the MZI by using MPS ($|\psi_j\rangle$) at port- a and vacuum ($|0\rangle$) at port- b (as shown in Fig. 3) for the parity and Z-detection schemes.

Our initial state of the system can be written as

$$|\psi\rangle_{in} = |\psi_j, 0, 0, 0\rangle_{a,b,E_a,E_b}. \quad (26)$$

Here $|\psi_j\rangle$ is the MPS at input mode a as given in Eq. (2) whereas b , E_a and E_b are the respective modes of the system in vacuum state as shown in Fig. 3. Then, using Eq. (14), the final state of the system at the output of MZI becomes

$$|\psi\rangle_{out} = N_j [A|K\rangle + B|L\rangle + C|M\rangle + D|N\rangle]_{a,b,E_a,E_b}. \quad (27)$$

Here $|K\rangle$, $|L\rangle$, $|M\rangle$, $|N\rangle$ are given in Eq. (A2). Eq. (27), contains the information about the unknown phase change during the probe evolution inside the interferometer and this will be used to calculate the resolution and phase sensitivity of the MZI in this case. For this purpose, we consider two measurement schemes defined in terms of two observables $\hat{\Pi}$ and \hat{Z} . The expectation values of $\hat{\Pi}$ and \hat{Z} are calculated in terms of the photon number probability as already discussed in Sections III C 1 & III C 2. To do this, the density operator for the final state of the system can be written as,

$$\hat{\rho}_{out} = |\psi\rangle_{out} \langle \psi|, \quad (28)$$

where $|\psi\rangle_{out}$ is given in Eq. (27). Then, using Eqs. (19) and (20), the probability of getting n photon numbers at port a is

$$P(n) = |N_j|^2 e^{-|\alpha|^2} \left(X e^{-p+|\alpha|^2} \frac{(p)^n}{n!} + V \left(e^{-iq} \frac{(-ip)^n}{n!} + c.c. \right) + Y \left(e^{q'} \frac{(-p)^n}{n!} + c.c. \right) \right). \quad (29)$$

Here

$$q = \left(|\alpha|^2 x - j \frac{\pi}{2} \right), q' = (-|\alpha|^2 x + ij\pi), \\ x = |t|^2 \cos^2 \left(\frac{\phi}{2} \right) + |r|^2, p = |\alpha|^2 |t|^2 \sin^2 \left(\frac{\phi}{2} \right). \quad (30)$$

Also, V , X and Y are given in Eq. (5).

A. Parity detection

In parity detection, the parity operator, $\hat{\Pi}$, divides the photon counting data $\{n, m\}$ into binary outcomes \pm , according to the even or odd number of photons at the

output port. So, the probability of getting an even or odd number of photons is

$$P(\pm) = |N_j|^2 e^{-|\alpha|^2} \left(\frac{1}{2} X e^{|\alpha|^2} (1 \pm e^{-2p}) + V(\cos(q+p) \pm \cos(q-p)) + Y e^{-|\alpha|^2} ((1 \pm e^{2p}) \cos(j\pi)) \right). \quad (31)$$

Here, p , q , q' are defined in Eq. (30). Therefore, from Eq. (21), the outcome of the parity measurement for the system can be written as

$$\langle \hat{\Pi} \rangle = |N_j|^2 e^{-|\alpha|^2} (X e^{-(2p-|\alpha|^2)} + 2V \cos(q-p) + Y e^{(2p-|\alpha|^2)} \cos(j\pi)). \quad (32)$$

This result in Eq. (32) will be used to calculate the resolution and phase sensitivity.

In direct detection, the resolution of the system depends on the ‘full width at half maximum (FWHM)’ of the intensity signal, i.e., $\Delta x \propto \text{FWHM}$. So, here, we follow the FWHM approach for observing the resolution of the system in six different cases of input states (as mentioned in Section II A) of the MZI.

Variation of $\langle \hat{\Pi} \rangle$ with respect to ϕ for different values of $|\alpha|^2$ is shown in Fig. 4. We can see that the foldness of ECSS, $\text{MPS}_{j=0}$, $\text{MPS}_{j=1}$, $\text{MPS}_{j=2}$ and $\text{MPS}_{j=3}$ increases by one w.r.t. coherent state. Wang *et al.* [30] found two-fold super-resolution by using even coherent superposition state (ECSS) as compared to CS in the lossless and noiseless cases. So, our focus is to study the FWHM of all six states. We can see that the width of the peaks decreases on increasing the photon number, i.e., on increasing $|\alpha|^2$, FWHM decreases. In order to compare the variation of FWHM with $|\alpha|^2$ for the different six cases and which one gives better resolution in comparison to the others, we plot Fig. 5(a). We can see that, $\text{MPS}_{j=0}$ shows the minimum FWHM with respect to other states for the lower values of $|\alpha|^2$ in parity measurement. While, for larger values of $|\alpha|^2 (> 5)$, all the states are giving the same FWHM and it is because of mean photon number variation in the state with $|\alpha|^2$ (Fig. 1). To see the effect of photon loss on the FWHM, we plot a graph between FWHM and photon loss (in terms of reflectivity (r) of the fictitious beam splitter shown in Fig. 3) by considering the mean photon number $N = 3$ in Fig. 5(b). We can see that, also in the lossy case the FWHM of the $\text{MPS}_{j=0}$ gives better results than other states. So, we can conclude that $\text{MPS}_{j=0}$ performs better resolution than ECSS in both lossless and lossy conditions.

In order to calculate the phase sensitivity ($\Delta\phi$) of MZI for parity detection, we use the Eq. (22). From Eq. (32), we can write

$$\frac{\partial \langle \hat{\Pi} \rangle}{\partial \phi} = |N_j|^2 e^{-|\alpha|^2} (-2p' X e^{-(2p-|\alpha|^2)} + 4V p' \sin(q-p) + 2p' Y e^{(2p-|\alpha|^2)} \cos(j\pi)). \quad (33)$$

Where $p' = \frac{1}{2} |\alpha|^2 |t|^2 \sin^2 \phi$, $x' = -\frac{1}{2} |t|^2 \sin^2 \phi$. So, in order to see the variation in phase sensitivity, we plot the $\Delta\phi/SNL$ versus ϕ for all six states in (a) lossless and (b) lossy conditions. From Fig. 6(a), we can see that all the states saturate the SNL. But in terms of the broader phase range (here, from $-\pi$ to π), $\text{MPS}_{j=1}$ (black solid lines) performs better as compared to all other states. Further, considering loss (i.e., varying r), we plot the $\Delta\phi/SNL$ vs. r by fixing $\phi = 0.02$ (Fig. 6(b)). Under lossy cases, we found that the phase sensitivity of all the states decreases in the same way.

B. Z - detection

For Z -detection, we calculate the zero non-zero photon counting probability at the output port. Therefore, from Eq. (24), we can write

$$\langle \hat{Z} \rangle = |N_j|^2 (X e^{-p} + 2e^{-|\alpha|^2} V \cos(q) + Y e^{-|\alpha|^2(1+x)} \cos(j\pi)). \quad (34)$$

Now, with the help of $\langle \hat{Z} \rangle$ operator as given in Eq. (34), we calculate the resolution and phase sensitivity.

For the resolution with Z -detection, we are plotting $\langle \hat{Z} \rangle$ with respect to ϕ by taking different values of $|\alpha|^2$ as shown in Fig. 7. Here, we observe that the FWHM of the signal decreases by increasing $|\alpha|^2$. Further, for comparing the values of FWHM of all six cases, we plot FWHM with $|\alpha|^2$ as shown in Fig. 8(a). We can see that, $\text{MPS}_{j=0}$ shows the minimum FWHM with respect to other states on increasing $|\alpha|^2$ similar to the parity detection and for larger values of $|\alpha|^2 (> 5)$, all the states give the same FWHM because of large values of $|\alpha|^2$ (Fig. 1). To see the loss effect on the FWHM, we have plotted a graph between FWHM and r (reflectivity of the fictitious beam splitter shown in Fig. 3) by considering $N = 3$ in Fig. 8(b). We found that in the lossy case, $\text{MPS}_{j=0}$ performs better than other states. So, we can conclude that $\text{MPS}_{j=0}$ gives better resolution as compared to all other states.

To calculate the phase sensitivity ($\Delta\phi_z$) of MZI for Z -detection, we use the Eq. (25). From Eq. (34), we can write

$$\frac{\partial \langle \hat{Z} \rangle}{\partial \phi} = |N_j|^2 (-p' X e^{-p} + 2p' e^{-|\alpha|^2} V \sin(q) - Y |\alpha|^2 x' e^{-|\alpha|^2(1+x)} \cos(j\pi)). \quad (35)$$

To evaluate the variation in phase sensitivity, we plot the $\Delta\phi_z/SNL$ versus ϕ for all six states for Z -detection in both the lossless and lossy conditions. Fig. 9(a) shows the variations in the lossless case. We can see that all the states saturate SNL but in terms of broader phase range, here, from $-\pi$ to π , $\text{MPS}_{j=1}$ (black solid lines) gives better results as compared to all other states. Further, after considering loss (i.e., varying r), we plot the $\Delta\phi/SNL$ vs. r fixing $\phi = 0.02$, as shown in Fig. 9(b).

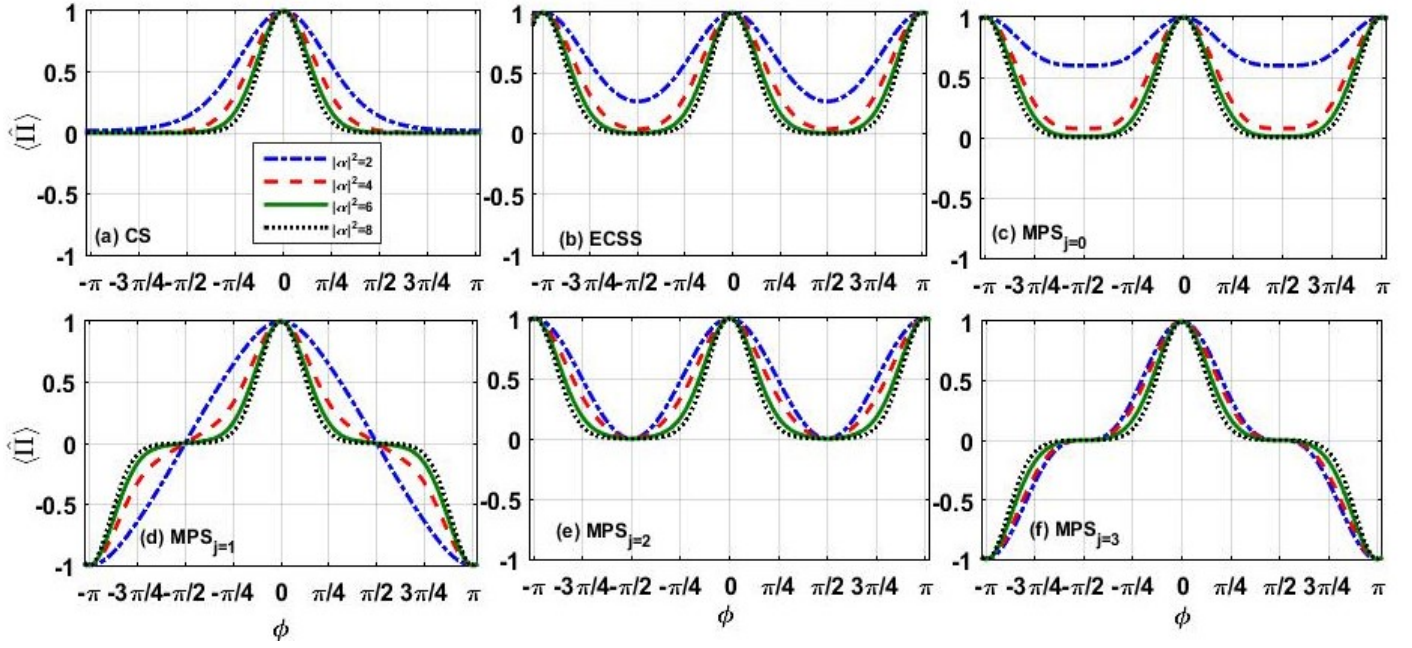


FIG. 4. This figure shows the variation of $\langle \hat{II} \rangle$ with respect to ϕ for different values of $|\alpha|^2$ for all six chosen states. We can see that the FWHM of the different states decreases with increasing $|\alpha|^2$.

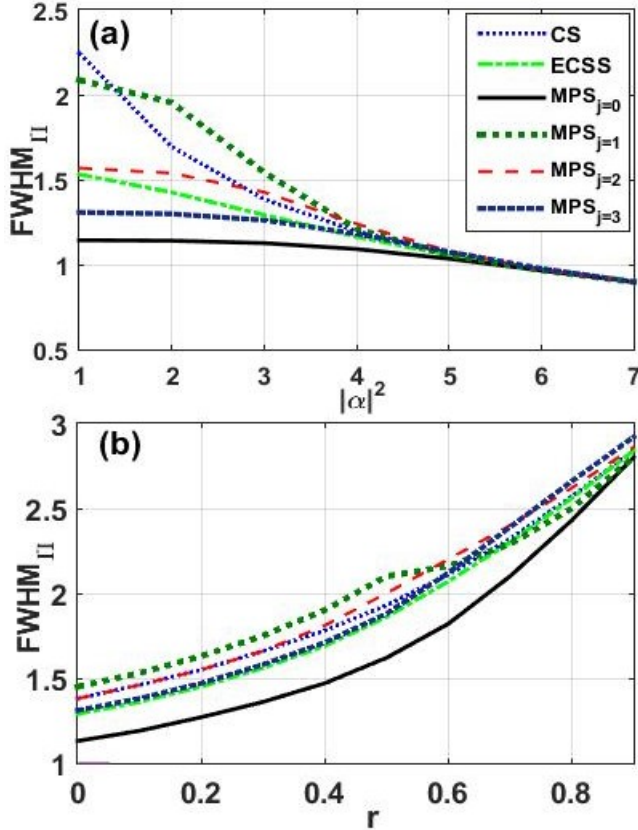


FIG. 5. (a) Plot shows the variation of FWHM with $|\alpha|^2$ for the different states and (b) shows the loss tolerance with mean photon number $N = 3$ in parity detection.

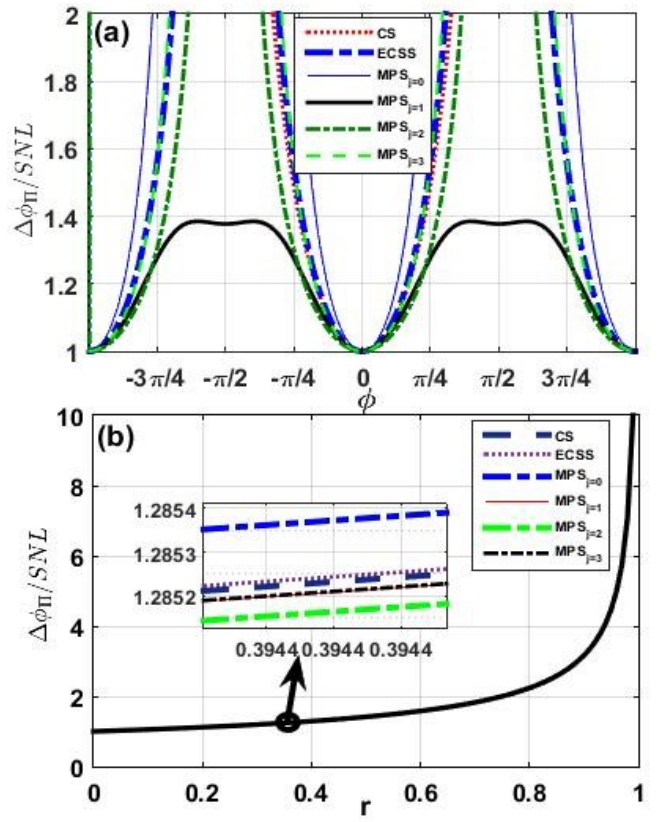


FIG. 6. (a) shows the phase sensitivity of the MZI in parity detection with $|\alpha|^2 = 2$. (b) shows $\Delta\phi/SNL$ vs. r variation with $\phi = 0.02$ and $|\alpha|^2 = 2$.

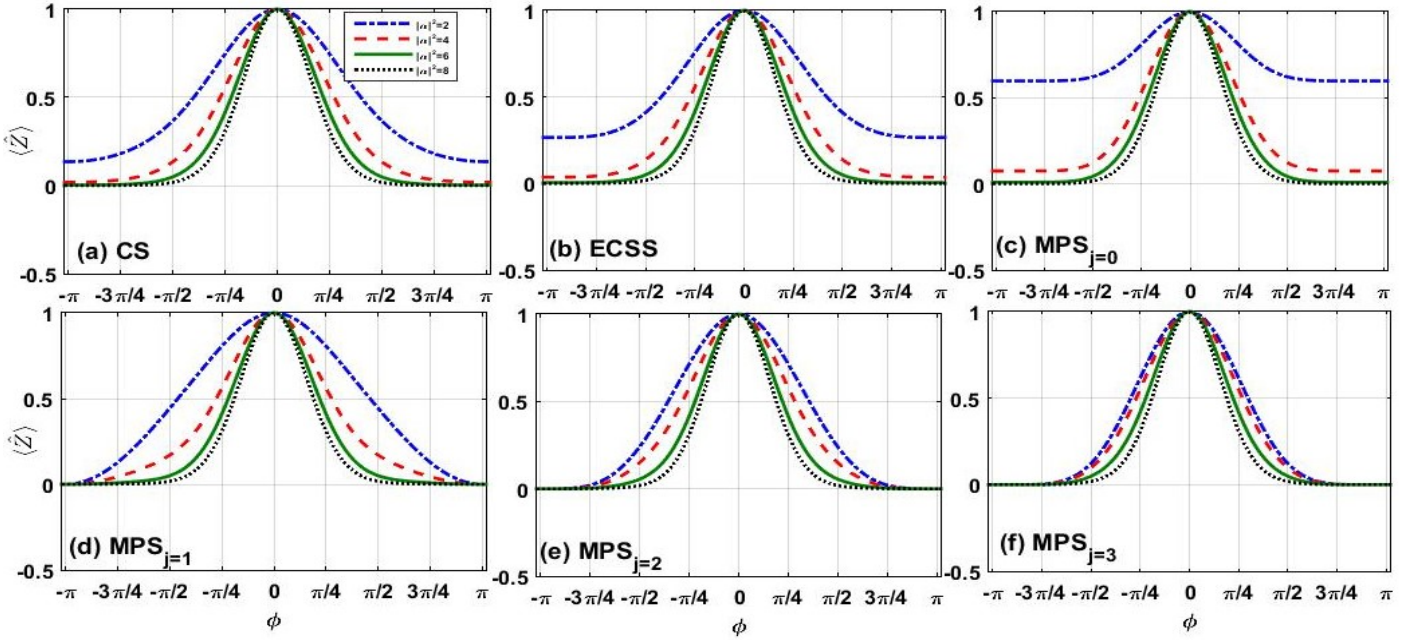


FIG. 7. The figure shows the variation of $\langle \hat{Z} \rangle$ with respect to ϕ for different values of $|\alpha|^2$ for the states CS, ECSS, $MPS_{j=0}$, $MPS_{j=1}$, $MPS_{j=2}$ and $MPS_{j=3}$. We can see that the FWHM of the different states decreases with increasing $|\alpha|^2$.

We found that all states behave similarly to the CS in lossy conditions.

We can summarize our results as given below:

For parity detection, with $|\alpha|^2 < 5$, foldness of ECSS, $MPS_{j=0}$, $MPS_{j=1}$, $MPS_{j=2}$ and $MPS_{j=3}$ increased by one w.r.t. CS (Fig. 4). FWHM of the $MPS_{j=0} < MPS_{j=3} < ECSS < MPS_{j=2} < CS < MPS_{j=1}$ (Fig. 5(a)). In the lossy case, FWHM of the $MPS_{j=0} < MPS_{j=3} \approx ECSS < MPS_{j=2} \approx CS < MPS_{j=1}$ (Fig. 5(b)). For $|\alpha|^2 > 5$, foldness of ECSS, $MPS_{j=0}$, $MPS_{j=1}$, $MPS_{j=2}$ and $MPS_{j=3}$ increases by one w.r.t. CS (Fig. 4). All the states are giving the same FWHM. For phase sensitivity, all the states saturate the SNL (Fig. 6(a)). $MPS_{j=1}$ performs better in broader phase range. Under lossy cases, all the states decrease in the same way (Fig. 6(b)).

For Z-detection, with $|\alpha|^2 < 5$, foldness of all states is same. FWHM of the $MPS_{j=0} < MPS_{j=3} < ECSS < MPS_{j=2} < CS < MPS_{j=1}$ (Fig. 8(a)). In the lossy case, FWHM of the $MPS_{j=0} < MPS_{j=3} \approx ECSS \approx CS < MPS_{j=2} < MPS_{j=1}$ (Fig. 8(b)). For $|\alpha|^2 > 5$, foldness of all the states is the same (Fig. 7). All the states are giving the same FWHM. All the states saturate SNL (Fig. 9(a)). $MPS_{j=1}$ performs better in broader phase range. Under lossy cases, all the states decrease in the same way (Fig. 9(b)).

V. SUPER-RESOLUTION AND SUPER-SENSITIVITY OF QUANTUM LIDAR WITH MPS AND COHERENT STATE AS INPUTS

In this section, we will discuss the resolution and phase sensitivity of the MZI by using MPS ($|\psi_j\rangle$) at input port-*a* and coherent state ($|\zeta\rangle$) at input port-*b* for parity and Z-detection schemes.

Our initial state of the system can be written as

$$|\psi'\rangle_{in} = |\psi_j, \zeta, 0, 0\rangle_{a,b,E_a,E_b}, \quad (36)$$

where mode *a* is in state $|\psi_j\rangle$ as given in Eq. (2), mode *b* is in coherent state $|\zeta\rangle$, and modes E_a & E_b are in vacuum states of the system as given in Fig. 3. Therefore, from Eq. (14), the final state of the system at the output of the interferometer can be written as

$$|\psi'\rangle_{out} = N_j (A|K'\rangle + B|L'\rangle + C|M'\rangle + D|N'\rangle)_{a,b,E_a,E_b}, \quad (37)$$

with, N_j is given in Eq. (4), A , B , C , D are given in Eq. (3) and $|K'\rangle$, $|L'\rangle$, $|M'\rangle$ and $|N'\rangle$ are given in Eq. (B2).

Eq. (37) gives the information about the final state of the system which includes the phase change and loss due to the environment. In this section, similar to the previous section, we are investigating the resolution and phase sensitivity of the MZI for parity and Z -detection schemes. Expectation values of $\hat{\Pi}$ and \hat{Z} are calculated in terms of the photon number probability as already discussed in Section III. Since from Eq. (19), we know that photon number probability can be written as

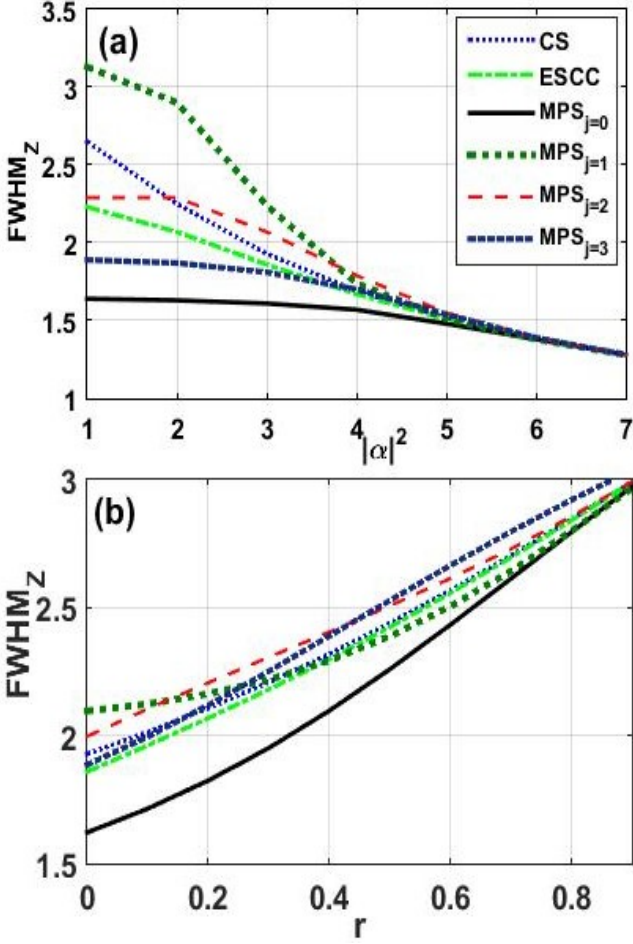


FIG. 8. (a) Plot shows the variation of FWHM with $|\alpha|^2$ for the different states in Z -detection and (b) shows the loss tolerance in Z -detection with $N = 3$.

$P(n, m) = \langle n, m | \hat{\rho}'_{out} | n, m \rangle$, where n and m are photon numbers on the output port a and b , respectively and $\hat{\rho}'_{out}$ is written as

$$\hat{\rho}'_{out} = |\psi'\rangle_{out} \langle \psi'|. \quad (38)$$

Here $|\psi'\rangle_{out}$ is given in Eq. (36). From Eq. (38), we can write the probability of getting m photon at port b (detailed equation is given in Eq. (B5) of Appendix B) and probability of getting even or odd number of photons at port a (detailed expression is given in Eq. (B6) of Appendix B).

A. Parity detection

In the parity detection scheme, the $\hat{\Pi}$ -operator divides the photon counting data $\{n, m\}$ into binary outcomes \pm , according to the even or odd number of photons at the output port. In Eq. (B6) of Appendix B, the probability of getting an even or odd number of photons is written. The expectation value of the parity operator for the system is written as

$$\begin{aligned} \langle \hat{\Pi} \rangle = & |N_j|^2 (|A|^2 (e^{-2G-W}) + (|B|^2 + |D|^2) e^{-2G} + |C|^2 (e^{-2G+W}) + e^{-(|\alpha|^2 + |\zeta|^2)} (2(|A||B| + |A||D|) (e^{S_1} \cos(T_1 - \frac{j\pi}{2})) \\ & + 2(|B||C| + |C||D|) (e^{S_2} \cos(T_2 - \frac{j\pi}{2})) + 2|B||D| (e^{(S_1-T_1)} \cos(2W - j\pi)) + 2|A||C| (e^{(S_1-T_1)} \cos(j\pi))). \end{aligned} \quad (39)$$

Here,

$$\begin{aligned} G &= |\alpha|^2 t^2 \sin^2(\frac{\phi}{2}) + |\zeta|^2 t^2 \cos^2(\frac{\phi}{2}), \\ T_1 &= V|\alpha|^2 - W, \quad T_2 = V|\alpha|^2 + W, \\ S_1 &= U|\zeta|^2 - W, \quad S_2 = U|\zeta|^2 + W, \\ U &= (-t^2 \cos(\phi) + r^2), \quad W = t^2 |\alpha| |\zeta| \sin(\phi), \\ V &= (t^2 \cos(\phi) + r^2). \end{aligned} \quad (40)$$

Firstly, we investigate the resolution of all the six states with coherent state ($|\zeta\rangle$) in another input port. We consider the different combinations of the photon numbers

on both inputs of the interferometer. In order to do the comparative study, we take an equal mean photon number (N) for all six states. Therefore, initially, we consider $|\zeta|^2 = 3$, $N = 3$ and see the variation of $\langle \hat{\Pi} \rangle$ with ϕ for all the six states (Fig. 10). Here, we see the improvement in the foldness of all the five states w.r.t. CS. In which $MPS_{j=3}$ gives higher foldness than the other four states (Fig. 10). If we increase the value of $|\zeta|^2$, we get the decrement in FWHM for all six states, as we can see in Fig. 11. To see the variation in FWHM with $|\zeta|^2$, we calculated the FWHM for all six states and plotted them in Fig. 12. We can see that, $MPS_{j=0}$, $MPS_{j=1}$ and ECSS gives minimum FWHM as compared to the other

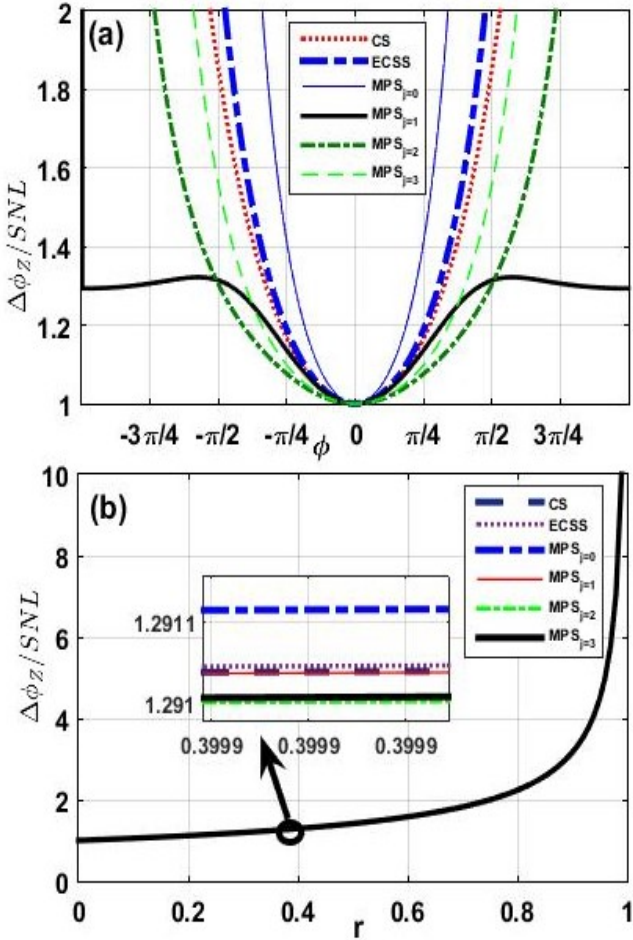


FIG. 9. (a) Shows the phase sensitivity shows $\Delta\phi/SNL$ vs. ϕ variation and (b) show $\Delta\phi/SNL$ vs. r with $\phi = 0.02$.

three states with increasing $|\zeta|^2$ (Fig. 12). From Fig. 5(a) and Fig. 12, we can say that MZI with MPS as one of the inputs having lower energy and another input port injected with a coherent state enhances the resolution of the MZI.

Now, we are interested in varying both $|\alpha|^2$ and $|\zeta|^2$, i.e., the energy variation in both inputs of the MZI. In order to discuss this, in detail, we divide it into four cases. (i) mean photon number of the MPS $N = 103$ and $|\zeta|^2 = 0$; (ii) $N = 3$ and $|\zeta|^2 = 100$; (iii) $N = 100$ and $|\zeta|^2 = 3$; and (iv) $N = 51$ and $|\zeta|^2 = 52$. Here, we take

care that energy input in all four cases should be equal. In Fig. 13, we can see that on varying the values of N and $|\zeta|^2$, foldness in the resolution increases in all five states as compared to the CS. For the fourth case (i.e., $N = 51$ and $|\zeta|^2 = 52$), we are getting the highest foldness as compared to the other three cases (Fig. 13). Here, it is important to note that, $MPS_{j=0}$, $MPS_{j=1}$, $MPS_{j=2}$ and $MPS_{j=3}$ give two extra peaks as compared to ECSS case (Fig. 14). This means we are getting extra folding in the resolution for the case of $MPS_{j=0,1,2,3}$ in comparison to the case of ECSS as the input state of the MZI. Thus, we

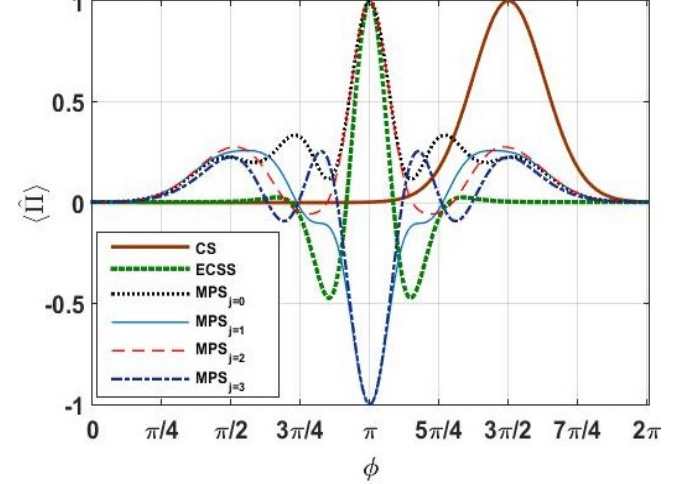


FIG. 10. Here the plots show the variation of all states with high photon numbers ($N = 3, |\zeta|^2 = 3$) in the input state in parity detection.

can conclude that an equal photon number in both input ports gives a better resolution than an unequal one.

In order to see the effect of loss on the foldness we consider an optimal value of $\phi = \pi$ and see the variation of $\langle \hat{\Pi} \rangle$ with r (grey inset of the Fig. 14). We can see that for $> 4\%$ loss we lose the foldness for the five states. While we still have the CS nature of the foldness for all the states. One more point here we mention that, in our analysis, we found that the loss tolerance property of the foldness of the states decreases with increasing photon number in the state.

In order to calculate the phase sensitivity ($\Delta\phi$) of MZI for parity detection, we use the Eq. (22). From Eq. (39), we can write

$$\begin{aligned} \frac{\partial \langle \hat{\Pi} \rangle}{\partial \phi} = & |N_j|^2 (|A|^2 e^{-2G-W} (-2G' - W') + (|B|^2 + |D|^2) e^{-2G} (-2G') + |C|^2 e^{-2G+W} (-2G' + W') \\ & + e^{-(|\alpha|^2 + |\zeta|^2)} (2(|A||B| + |A||D|) (e^{S_1 S'_1} \cos(T_1 - \frac{j\pi}{2}) - e^{S_1 T'_1} \sin(T_1 - \frac{j\pi}{2})) \\ & + 2(|B||C| + |C||D|) (e^{S_2 S'_2} \cos(T_2 - \frac{j\pi}{2}) - e^{S_2 T'_2} \sin(T_2 - \frac{j\pi}{2}))) \quad (41) \\ & + 2|B||D| (e^{(S_1 - T_1)} (S'_1 - T'_1) \cos(2W - j\pi) - 2W' e^{(S_1 - T_1)} \sin(2W - j\pi)) + 2|A||C| e^{(S_1 - T_1)} (S'_1 - T'_1) \cos(j\pi)) \end{aligned}$$

$$+ 2|B||D| (e^{(S_1 - T_1)} (S'_1 - T'_1) \cos(2W - j\pi) - 2W' e^{(S_1 - T_1)} \sin(2W - j\pi)) + 2|A||C| e^{(S_1 - T_1)} (S'_1 - T'_1) \cos(j\pi)) \Big).$$

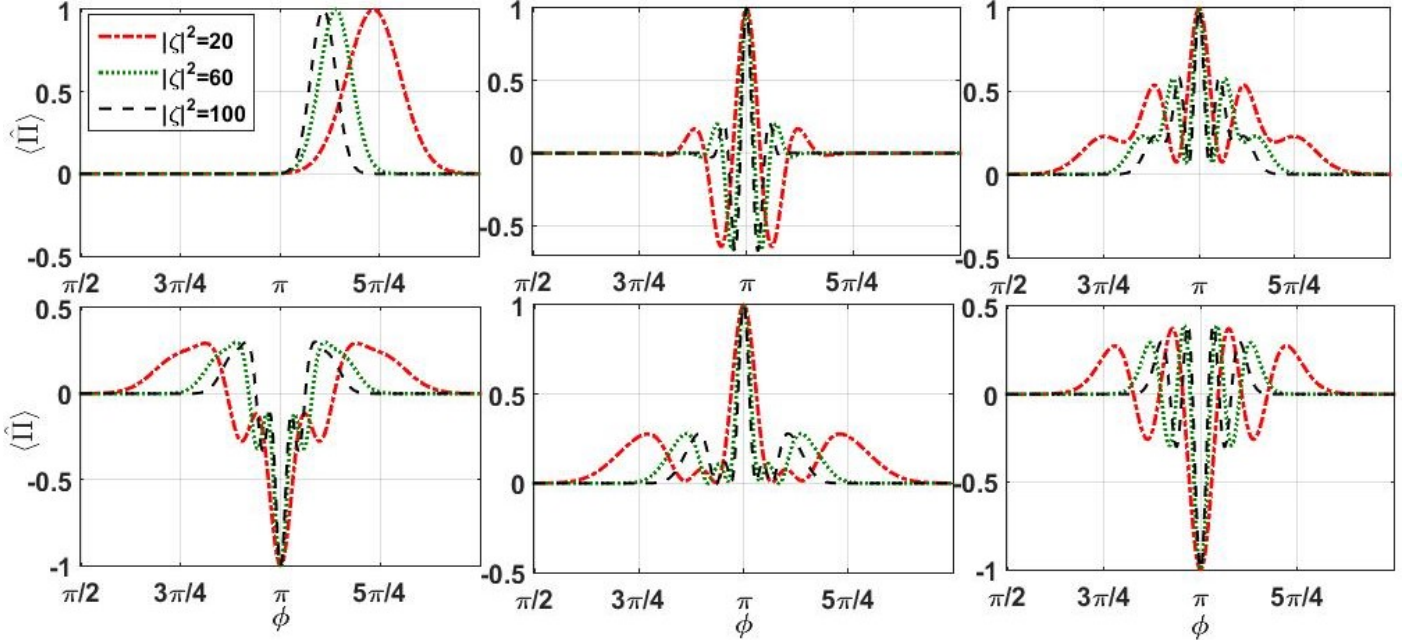


FIG. 11. These plots shows the variation of $\langle \hat{\Pi} \rangle$ w.r.t. ϕ for all six states with varying $|\zeta|^2$ with $N = 3$. On increasing the value of $|\zeta|^2$, we get the decrement in FWHM for all six states

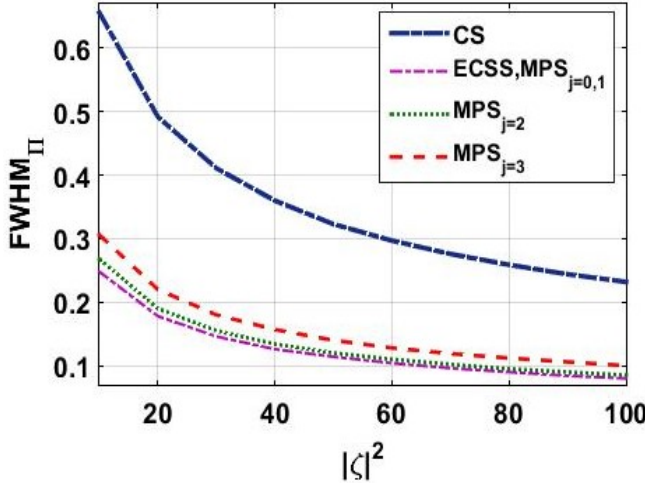


FIG. 12. The plots shows the variation of FWHM of all the six states with $|\zeta|^2$ having $N = 3$.

Here, G , W , S_1 , S_2 , T_1 are given in Eq. (40) and

$$\begin{aligned} G' &= \frac{1}{2}(|\alpha|^2 - |\zeta|^2)t^2 \sin(\phi), \quad T_1' = V'|\alpha|^2 - W', \\ T_2' &= V'|\alpha|^2 + W', \quad S_1' = U'|\zeta|^2 - W', \\ S_2' &= U'|\zeta|^2 + W', \quad U' = t^2 \sin(\phi), \\ W' &= t^2|\alpha||\zeta| \cos(\phi), \quad V' = -t^2 \cos(\phi). \end{aligned} \quad (42)$$

For the phase sensitivity, we see the variation $\Delta\phi/SNL$ with ϕ . Similar to the resolution part, we will discuss the results for different input photon variations. Firstly,

we consider two cases: (i) for $|\zeta|^2 = 2$, $|\alpha|^2 = 2$ and, (ii) for $|\zeta|^2 = 100$, $|\alpha|^2 = 2$. In both cases, we have found that $\Delta\phi/SNL$ beats the SNL for all the states except the CS (Fig. 15). This shows that MPS with CS ($|\zeta\rangle$) as the input of the MZI gives super phase sensitivity. Also, note that With a high photon number ($|\zeta|^2 = 100$) in the coherent state, we get the improvement in the phase sensitivity (Fig. 15). In the photon loss, we found that ECSS gives approximately 10% and the other four give approximately 5% photon loss (grey inset in Fig. 15(a)) in the first case($|\zeta|^2 = 2$, $|\alpha|^2 = 2$), and ECSS gives ap-

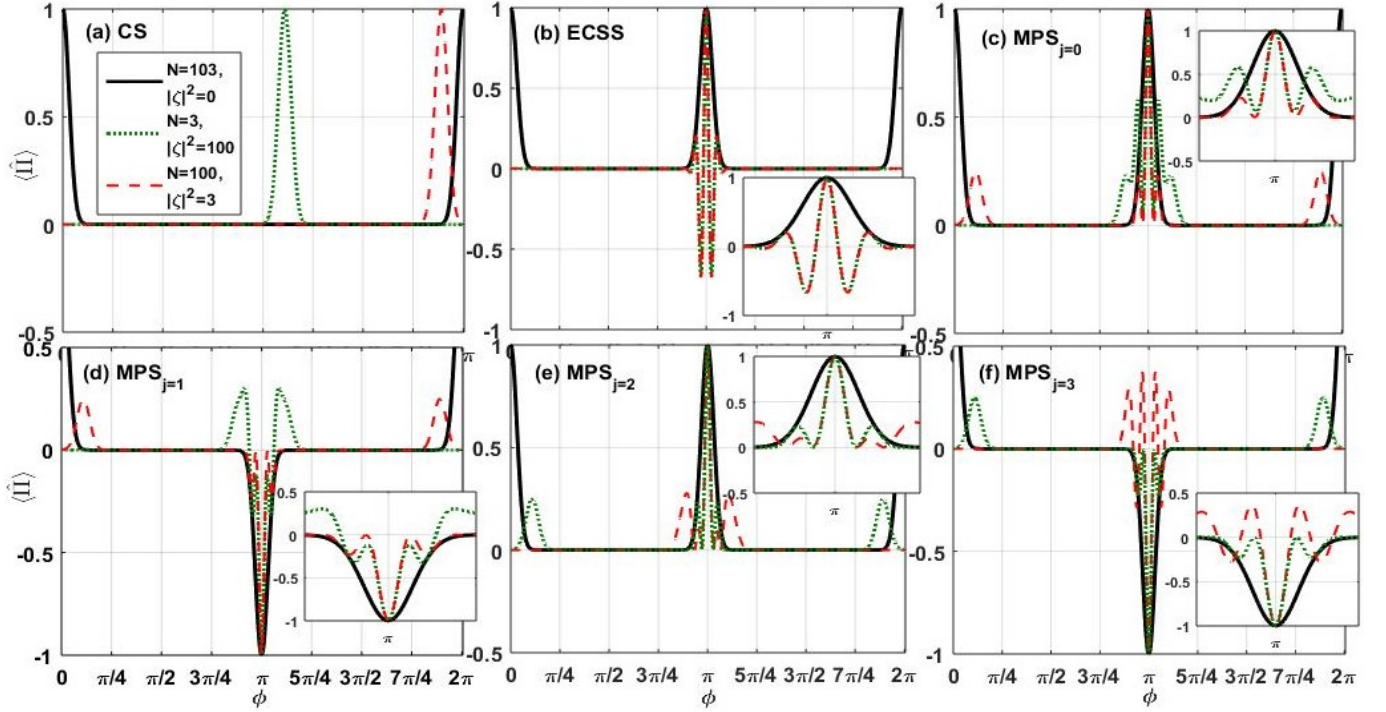


FIG. 13. These plots show the variation of all states with high photon numbers in the input state in parity detection.

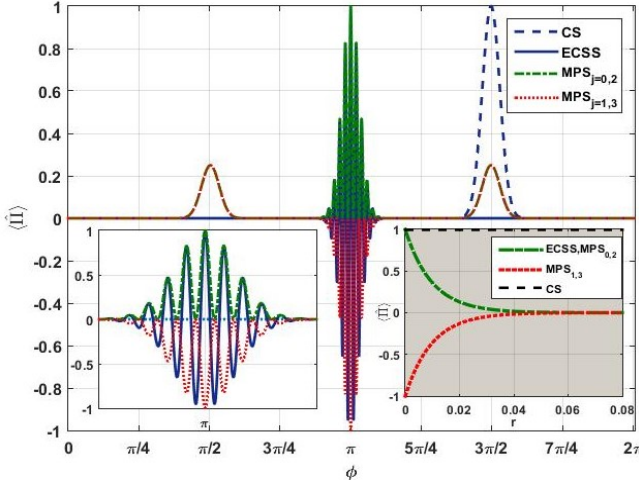


FIG. 14. Plots show the variation of $\langle \hat{\Pi} \rangle$ versus ϕ for all six states with $N = 51$, $|\zeta|^2 = 52$. As we can see if we put a nearly equal number of photons in coherent state and MPS then the foldness of the output signal increases as compared to MPS with a vacuum as an input. We can see that $MPS_{j=0,1,2,3}$ gives extra peaks in compare to ECSS.

proximately 20% and the other four give approximately 10% photon loss (grey inset in Fig. 15(b)) in the second case ($|\zeta|^2 = 100$, $|\alpha|^2 = 2$). Now, we consider the case in which $|\alpha|^2 = 51$, $|\zeta|^2 = 52$. We get a significant change in the phase sensitivity, as shown in Fig. 16. But in this case, we found a very small loss tolerance (grey inset in Fig. 16).

B. Z-detection

For Z -detection, we calculate the zero non-zero photon counting probability at the output port. Associated probabilities for $n = 0$ and $n \neq 0$ are given by $P(0)$ and $P(\emptyset) = 1 - P(0)$ as mentioned in section III C 2. Therefore, from Eq. (24), we can write

$$\begin{aligned} \langle \hat{Z} \rangle = & |N_j|^2 ((|A|^2 e^{(-G-W)} + (|B|^2 + |D|^2) e^{-G} + |C|^2 e^{(-G+W)}) + 2 e^{-(|\alpha|^2 + |\zeta|^2)} ((|A||B| \\ & + |A||D|) e^{(\frac{1}{2}(S_1) + \frac{1}{2}|\zeta|^2)} \cos(\frac{1}{2}(T_1 + |\alpha|^2) - \frac{j\pi}{2}) + (|B||C| + |C||D|) e^{(\frac{1}{2}(S_2) + \frac{1}{2}|\zeta|^2)} \cos(\frac{1}{2}(T_2 + |\alpha|^2) - \frac{j\pi}{2}) \\ & + |B||D| e^{(\frac{1}{2}(S_1 - T_1) + \frac{1}{2}(|\zeta|^2 - |\alpha|^2))} \cos(j\pi - W) + |A||C| e^{(\frac{1}{2}(S_1 - T_1) + \frac{1}{2}(|\zeta|^2 - |\alpha|^2))} \cos(j\pi))) \end{aligned} \quad (43)$$

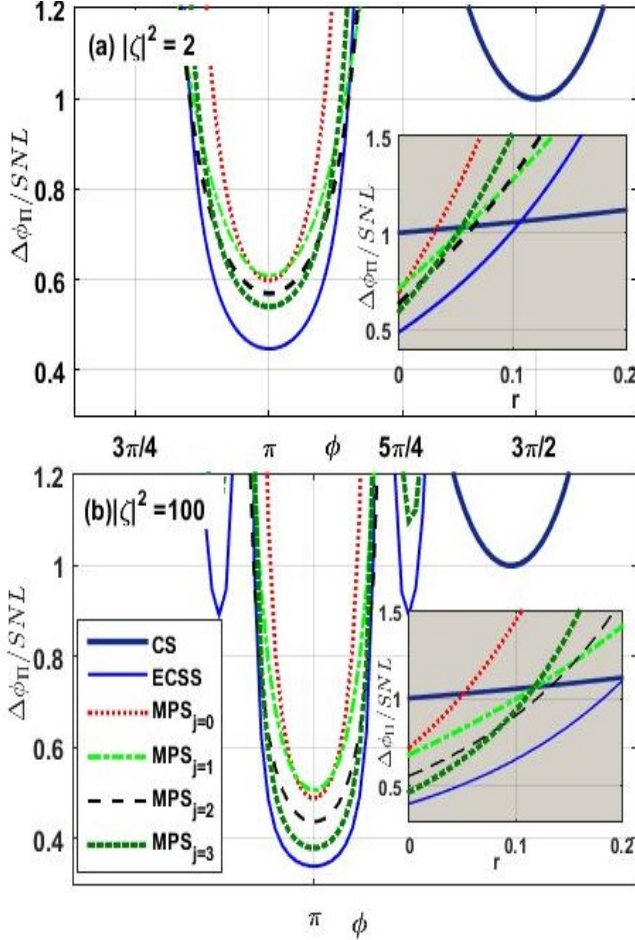


FIG. 15. These two plots show the variation of $\Delta\phi$ versus ϕ plot for all six chosen state. (a) shows the variation with $|\zeta|^2 = 2$ and $|\alpha|^2 = 2$, (b) shows the variation with $|\zeta|^2 = 100$ and $|\alpha|^2 = 2$.

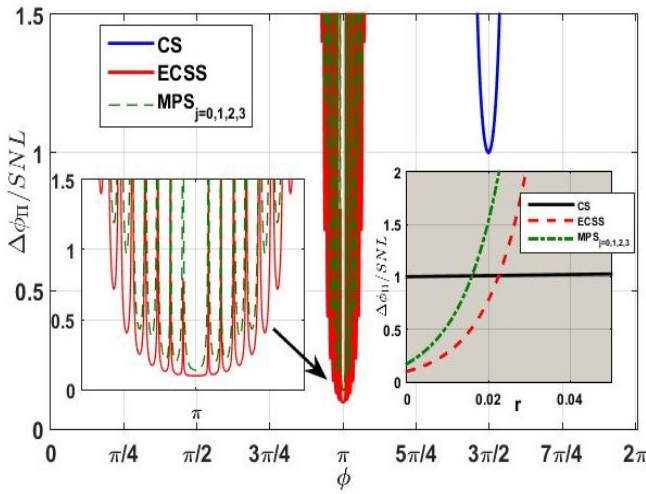


FIG. 16. Graphs show the variation of $\Delta\phi/\text{SNL}$ versus ϕ for all six states with $N = 51$ $|\zeta|^2 = 52$. We can see that for ECSS, $\text{MPS}_{j=0,1,2,3}$, phase sensitivity beats the SNL. In the grey inset, we show the effect of loss on the phase sensitivity.

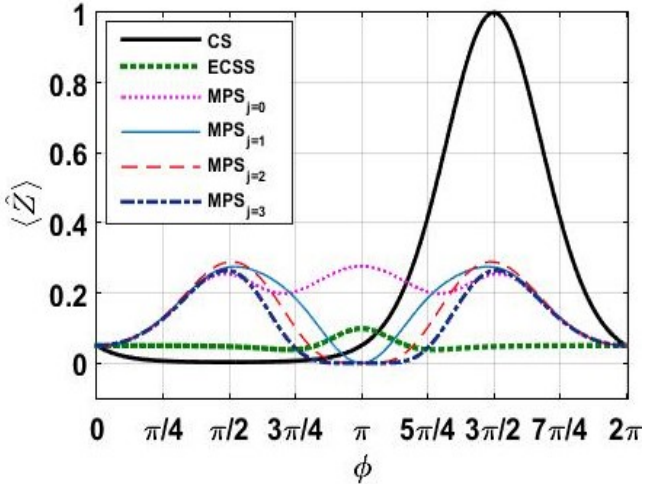


FIG. 17. Plots show the variation of $\langle \hat{Z} \rangle$ versus ϕ with $|\zeta|^2 = 3$ and $N = 3$. We can see that $MPS_{j=0,1,2,3}$ give foldness greater than the CS, and ECSS

So, with the help of $\langle \hat{Z} \rangle$, we calculate the resolution and phase sensitivity. In order to discuss the resolution for all the six states with CS ($|\zeta\rangle$) as the second input of the interferometer, we plotted $\langle \hat{Z} \rangle$ versus ϕ .

Firstly, we consider the $N = 3$, $|\zeta|^2 = 3$ and we find that $MPS_{j=0,1,2,3}$ give foldness greater than the CS, and ECSS, as shown in Fig. 17. As we increase the value of $|\zeta|^2$, FWHM for all the six states decreases (Fig. 18).

Now, we are interested in varying the values of $|\alpha|^2$ and $|\zeta|^2$ to see the effect on the resolution of the MZI. In Fig. 19, we can see the plots of $\langle \hat{Z} \rangle$ versus ϕ for four different cases of mean photon number (N) and $|\zeta|^2$. From Fig. 19, we can easily see that $MPS_{j=0}$, $MPS_{j=1}$, $MPS_{j=2}$ and $MPS_{j=3}$ performs better than ECSS and CS in all the situation except when $N = 103$ and $|\zeta|^2 = 0$. Here, we notice that as we increase the value of N we found that, for higher values, $MPS_{j=0,1,2,3}$ gives approximately the same results. Here for the case of $N = 51$ and $|\zeta|^2 = 52$, we found that $MPS_{j=0,1,2,3}$ gives 2 fold resolution as compared to CS in loss also (Fig. 20). ECSS performs worse in lossless as well as in lossy conditions (Fig. 20). So, in conclusion, we can say that $MPS_{j=0,1,2,3}$ gives better results than ECSS and CS for Z -detection. Since Z -detection is more feasible than parity detection, we can say that with MPS we are getting better results in comparison to parity detection with CS as one of the inputs of MZI.

In order to calculate the phase sensitivity ($\Delta\phi$) of MZI for Z -detection, we use the Eq. (25). From Eq. (43), we can write

$$\begin{aligned}
 \frac{\partial \langle \hat{Z} \rangle}{\partial \phi} = & |N_j|^2 ((|A|^2 e^{(-G-W)} (-G' - W') + (|B|^2 + |D|^2) e^{-G} (-G') + |C|^2 e^{(-G+W)} (-G' + W')) \\
 & + 2e^{-(|\alpha|^2 + |\zeta|^2)} ((|A||B| + |A||D|) (\frac{1}{2} S'_1 e^{(\frac{1}{2} S_1 + \frac{1}{2} |\zeta|^2)} \cos(\frac{1}{2}(T_1 + |\alpha|^2) - \frac{j\pi}{2}) - \frac{1}{2} T'_1 e^{(\frac{1}{2} S_1 + \frac{1}{2} |\zeta|^2)} \sin(\frac{1}{2}(T_1 + |\alpha|^2) - \frac{j\pi}{2})) \\
 & + (|B||C| + |C||D|) (\frac{1}{2} S'_2 e^{(\frac{1}{2} S_2 + \frac{1}{2} |\zeta|^2)} \cos(\frac{1}{2}(T_2 + |\alpha|^2) - \frac{j\pi}{2}) - \frac{1}{2} T'_2 e^{(\frac{1}{2} (S_2) + \frac{1}{2} |\zeta|^2)} \sin(\frac{1}{2}(T_2 + |\alpha|^2) - \frac{j\pi}{2})) \\
 & + |B||D| (\frac{1}{2} (S'_1 - T'_1) e^{(\frac{1}{2}(S_1 - T_1) + \frac{1}{2}(|\zeta|^2 - |\alpha|^2))} \cos(j\pi - W) + W' e^{(\frac{1}{2}(S_1 - T_1) + \frac{1}{2}(|\zeta|^2 - |\alpha|^2))} \sin(j\pi - W)) \\
 & + \frac{1}{2} (S'_1 - T'_1) |A||C| e^{(\frac{1}{2}(S_1 - T_1) + \frac{1}{2}(|\zeta|^2 - |\alpha|^2))} \cos(j\pi))). \tag{44}
 \end{aligned}$$

In order to discuss the result, we consider two cases: (i) $|\alpha|^2 = 2$, $|\zeta|^2 = 2$; (ii) $|\alpha|^2 = 2$, $|\zeta|^2 = 100$. We plot the $\Delta\phi/SNL$ versus ϕ for both the cases (Fig. 21). From Fig. 21, we can see that we get better phase sensitivity in both cases for CS and $MPS_{j=1}$.

We can summarize our results as given below:

For parity detection, with $N = 3$, $|\zeta|^2 = 3$, foldness of $MPS_{j=3} > MPS_{j=2} \approx MPS_{j=1} \approx ECSS \approx MPS_{j=0} > CS$ (Fig. 10). For $N = 3$, $|\zeta|^2 = 20, 60, 100$, FWHM for all six states decreases (Fig. 11). $MPS_{j=0} \approx MPS_{j=1} \approx ECSS < MPS_{j=2} < MPS_{j=3} < CS$ (Fig. 12). For $N > 3$, $|\zeta|^2 > 10$, foldness in the resolution increases in all four MPS and ECSS as compared to the CS (Fig. 13). For $N = 51$, $|\zeta|^2 = 52$, getting the highest foldness for all five states (Fig. 14). Foldness of $MPS_{j=0} =$

$MPS_{j=1} = MPS_{j=2} = MPS_{j=3} > ECSS > CS$ (Fig. 14). In the lossy scenario, all states show the loss tolerance of $< 4\%$ (grey inset in Fig. 14). Except CS all the states beat the SNL (Fig. 15). In case of loss, for lower photon number ($|\zeta|^2 = 2$, $|\alpha|^2 = 2$), ECSS shows 10% and MPS give approximately 5% photon loss (grey inset in Fig. 15(a)). While for higher photons numbers in CS, ($|\zeta|^2 = 100$, $|\alpha|^2 = 2$) ECSS shows 20% and MPS shows approximately 10% photon loss (grey inset in Fig. 15(b)). In case of $N = 51$ $|\zeta|^2 = 52$ loss tolerance decreases (grey inset of Fig. 16).

For Z -detection, with $|\alpha|^2 = 3$, $|\zeta|^2 = 3$ $MPS_{j=1}$, $MPS_{j=2}$ and $MPS_{j=3}$ give greater foldness than the CS, ECSS, and $MPS_{j=0}$ (Fig. 17). Increasing $|\zeta|^2 : 20, 60, 100$ and fixing $N = 3$, foldness of $MPS_{j=1}$, $MPS_{j=2}$ and

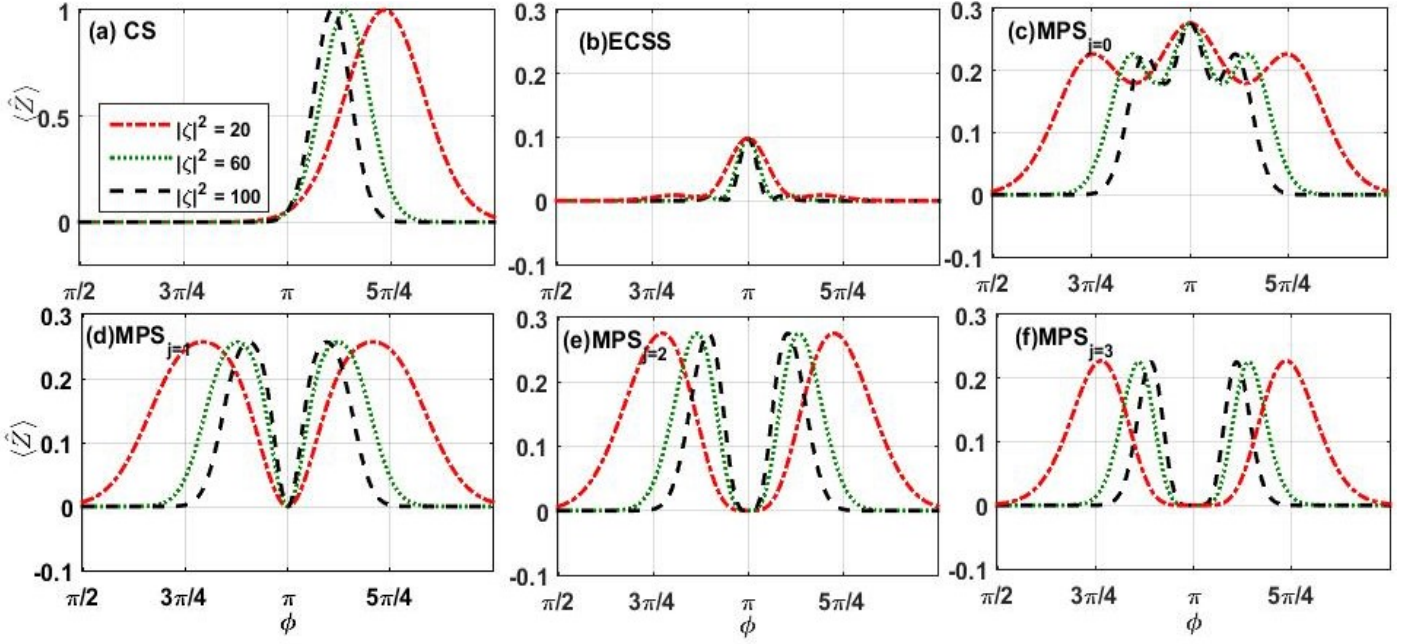


FIG. 18. These plots show the variation of $\langle Z \rangle$ w.r.t. ϕ for all six states with varying $|\zeta|^2$ and $N = 3$. We can see that on increasing the value of $|\zeta|^2$, FWHM for all the six states decrease.

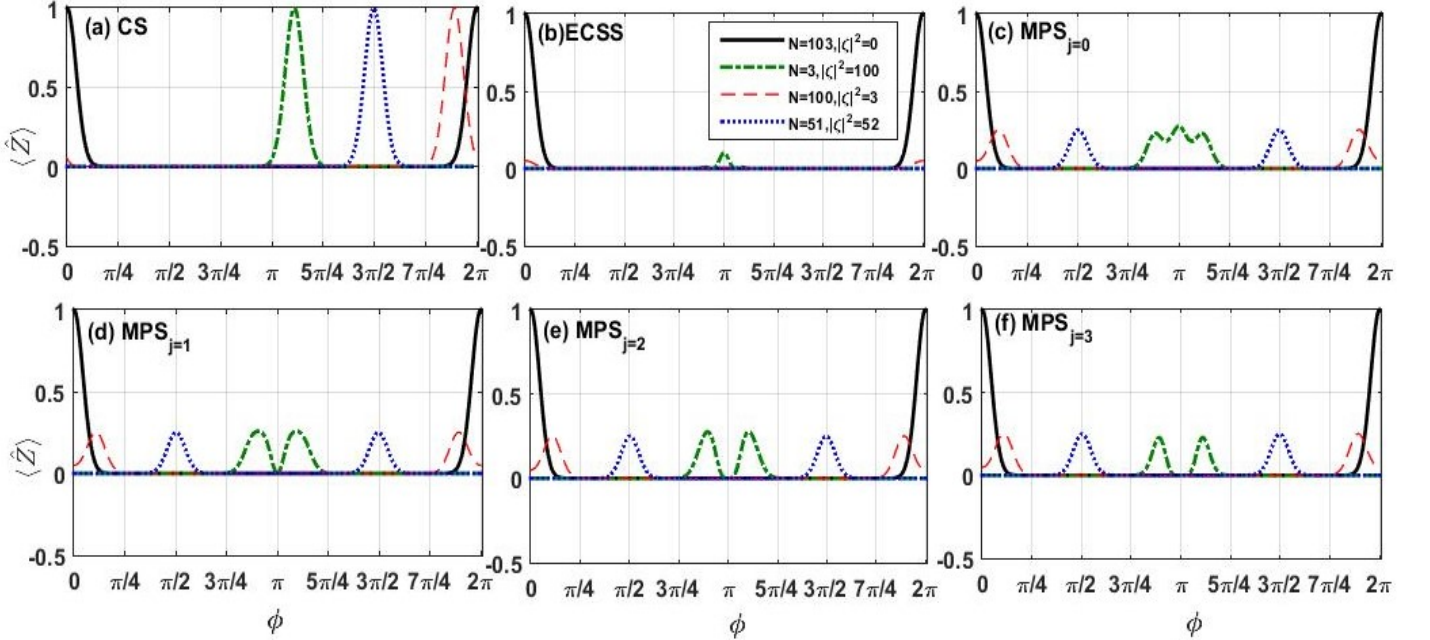


FIG. 19. These plots show the variation of all six states with high photon numbers in the input state. Here all four MPS show increased foldness but the peak height is too small. We can see that, in this case, the performance of ECSS is very poor.

MPS $_{j=3}$ becomes two (Fig. 18). For CS, ECSS, and MPS $_{j=0}$, it is one (range of ϕ from 0 to 2π). We get the decrement in FWHM for all six cases (Fig. 18). varying N and $|\zeta|^2$ MPS $_{j=0,1,2,3}$, performs better than ECSS and CS in all the situation except when $N = 103$ and $|\zeta|^2 = 0$ Fig. 19. For $N = 51$ and $|\zeta|^2 = 52$, MPS $_{j=0,1,2,3}$ gives 2 fold resolution as compared to CS in lossless as well as

lossy condition (Fig. 20). From Fig. 21, we can see that we get better phase sensitivity in both cases for CS and MPS $_{j=1}$.

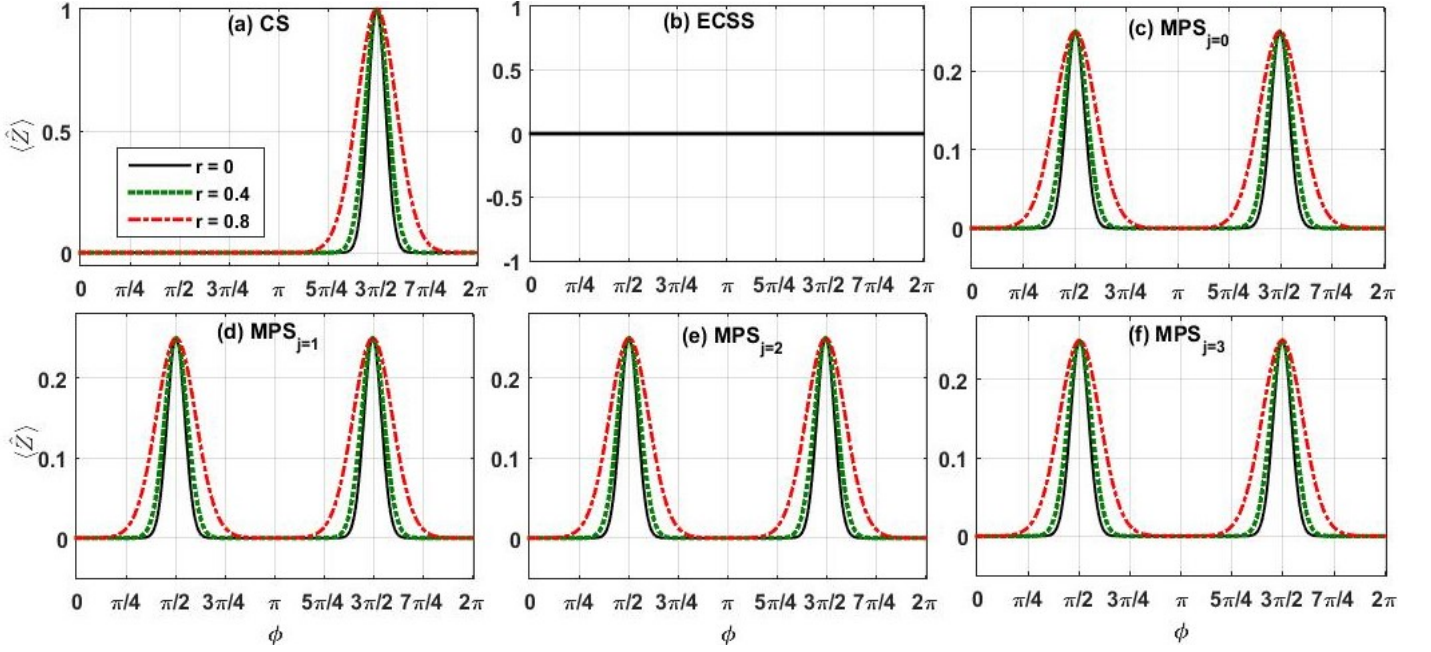


FIG. 20. These plots show the variation of all six states with $N = 51$, $|\zeta|^2 = 52$ in the input state in lossy condition. Here all four MPS show 2-fold peaks than CS in lossless ($r = 0$) as well as in lossy ($r \neq 0$) conditions. The performance of ECSS is very poor also in this case.

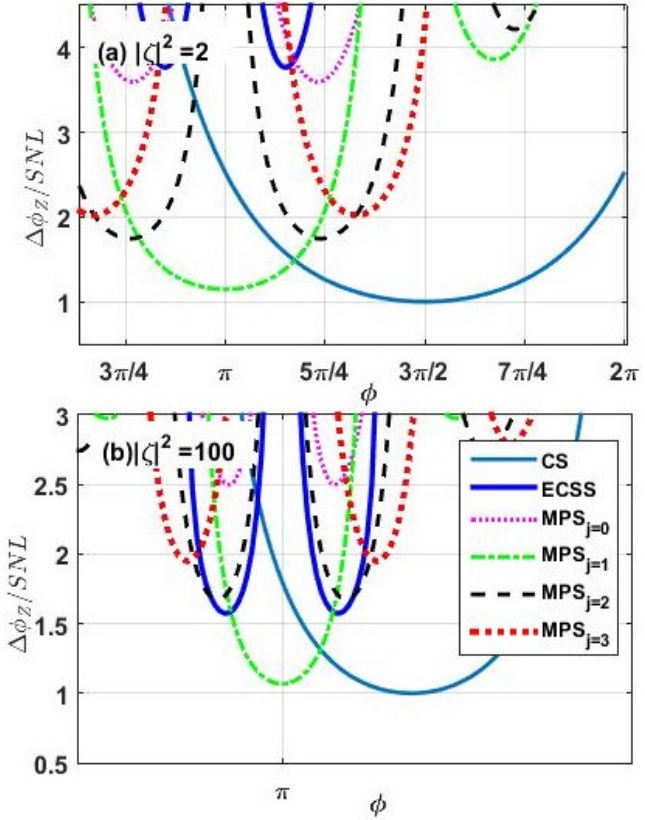


FIG. 21. Plots show the variation of $\Delta\phi/SNL$ versus ϕ for all six states. (a) Shows the variation with $|\alpha|^2 = 2$, $|\zeta|^2 = 2$, and (b) shows the variation with $|\alpha|^2 = 2$, $|\zeta|^2 = 100$.

VI. DISCUSSION AND CONCLUSIONS

In this paper, we have investigated the enhancement in phase sensitivity and resolution in MZI-based Quantum LiDAR by employing multi-photon states (MPSs) denoted as $MPS_{j=0,1,2,3}$, vacuum state $|0\rangle$, and coherent state $|\zeta\rangle$ as inputs to the Mach-Zehnder interferometer (MZI). We have explored two measurement schemes: binary outcome parity photon counting and binary outcome zero non-zero photon counting to analyze the performance.

In Section IV, we specifically focused on the case of $MPS_{j=0}$ as the input, which demonstrated superior resolution compared to other states for both detection scenarios (Fig. 5(a) and Fig. 8(a)). In the presence of loss, $MPS_{j=0}$ outperformed other states (Fig. 5(b) and Fig. 8(b)). Regarding phase sensitivity, all states reached the standard quantum limit (SNL). However, for a wide range of phase values, $MPS_{j=1}$ exhibited enhanced performance (Fig. 6(a) and Fig. 9(a)). In lossy conditions, all states degraded similarly (Fig. 6(b) and Fig. 9(b)).

In Section V, we substituted the vacuum with a coherent state as the input. In the low-energy region, the interferometer's resolution improved for $MPS_{j=0,1,2,3}$ states and the ECSS relative to the coherent state in both detection schemes (Fig. 10, Fig. 17). In the high-energy region, during parity detection, achieving approximately equal mean photon numbers in both inputs resulted in significant resolution enhancement (Fig. 13 and Fig. 14). Moreover, in the high-energy range, $MPS_{j=0,1,2,3}$ provided additional resolution enhancement compared to the

ECSS (Fig. 11, Fig. 13, and Fig. 14). Concerning phase sensitivity, all states except the coherent state surpassed the SNL (Fig. 15). In terms of loss tolerance, for low photon numbers in CS, the ECSS exhibited a loss tolerance of less than 10%, while $\text{MPS}_{j=0,1,2,3}$ states showed a loss tolerance of less than 5% compared to the coherent state (grey inset in Fig. 15(a)). While for higher photons numbers in CS, ECSS shows 20% and MPS shows approximately 10% photon loss (grey inset in Fig. 15(b)). However, with higher photon numbers, loss tolerance decreased (grey inset of Fig. 16). In the case of the Z-detection scheme, $\text{MPS}_{j=0,1,2,3}$ outperformed the ECSS and coherent state in terms of resolution (Fig. 17, Fig. 18, and Fig. 19). For higher and equal numbers of photons in the input state we found that $\text{MPS}_{j=0,1,2,3}$ gives 2 fold resolution as compared to CS in lossless as well as lossy conditions (Fig. 20). $\text{MPS}_{j=0,1,2,3}$ gives better results than ECSS and CS for Z-detection. As for phase sensitivity, the coherent state and $\text{MPS}_{j=1}$ yielded better results (Fig. 21).

In summary, the four multi-photon states ($\text{MPS}_{j=0,1,2,3}$) introduced by Mishra et al. [1] exhibit super-resolution and enhanced phase sensitivity. Since with MPS we are getting super sensitivity so we get better measurements in ranging also.

These states outperform the coherent state in most scenarios and also surpass the even coherent superposition state (ECSS) [30, 48, 49] in many cases. The experimental scheme for generating these multi-photon states has been proposed in [1]. Consequently, multi-photon states hold promise as an alternative nonclassical resource for quantum imaging and quantum sensing applications, such as in quantum LiDAR.

ACKNOWLEDGMENTS

PS acknowledges UGC for the UGC Research Fellowship. PS would like to thank Mr. Gaurav Shukla for his useful comments and suggestions. DKM acknowledges financial support from the Science & Engineering Research Board (SERB), New Delhi for CRG Grant (CRG/2021/005917) and Incentive Grant under Institution of Eminence (IoE), Banaras Hindu University, Varanasi, India. MKM would like to thank Shri Nilesh M. Desai (Director, SAC, Ahmedabad) and Dr. Rashmi Sharma for their encouragement and support.

Appendix A: calculation with MPS and vacuum state as inputs

The final state of the system at the output of MZI

$$|\psi\rangle_{out} = N_j [A|K\rangle + B|L\rangle + C|M\rangle + D|N\rangle]_{a,b,E_a,E_b}, \quad (\text{A1})$$

where, N_j is given in Eq. (4), A, B, C, D are given in Eq. (3) and $|K\rangle, |L\rangle, |M\rangle$ and $|N\rangle$ are given as

$$\begin{aligned} |K\rangle &= |k_1, k_2, k_3, k_4\rangle, \\ |L\rangle &= |l_1, l_2, l_3, l_4\rangle, \\ |M\rangle &= |m_1, m_2, m_3, m_4\rangle, \\ |N\rangle &= |n_1, n_2, n_3, n_4\rangle. \end{aligned} \quad (\text{A2})$$

With

$$\begin{aligned} k_1 &= \alpha\vartheta, \quad k_2 = \alpha\varsigma, \quad k_3 = \bar{r}\alpha e^{i\phi}, \quad k_4 = i\bar{r}\alpha, \\ l_1 &= \beta\vartheta, \quad l_2 = \beta\varsigma, \quad l_3 = \bar{r}\beta e^{i\phi}, \quad l_4 = i\bar{r}\beta, \\ m_1 &= \gamma\vartheta, \quad m_2 = \gamma\varsigma, \quad m_3 = \bar{r}\gamma e^{i\phi}, \quad m_4 = i\bar{r}\gamma, \\ n_1 &= \delta\vartheta, \quad n_2 = \delta\varsigma, \quad n_3 = \bar{r}\delta e^{i\phi}, \quad n_4 = i\bar{r}\delta, \end{aligned} \quad (\text{A3})$$

where, $\vartheta = ite^{\frac{i\phi}{2}} \sin\left(\frac{\phi}{2}\right)$, $\varsigma = ite^{\frac{i\phi}{2}} \cos\left(\frac{\phi}{2}\right)$ and $\bar{r} = ir/\sqrt{2}$. The density operator ($\hat{\rho}_{out}$) for the final state of the system is written as

$$\begin{aligned} \hat{\rho}_{out} = |\psi\rangle_{out} \langle \psi| &= |N_j|^2 (|A|^2|K\rangle\langle K| \\ &+ |B|^2|L\rangle\langle L| + |C|^2|M\rangle\langle M| + |D|^2|N\rangle\langle N| \\ &+ AB^*|K\rangle\langle L| + BA^*|L\rangle\langle K| + AC^*|K\rangle\langle M| \\ &+ CA^*|M\rangle\langle K| + AD^*|K\rangle\langle N| + DA^*|N\rangle\langle K| \\ &+ BC^*|L\rangle\langle M| + CB^*|M\rangle\langle L| + BD^*|L\rangle\langle N| \\ &+ DB^*|N\rangle\langle L| + CD^*|M\rangle\langle N| + DC^*|N\rangle\langle M|). \end{aligned} \quad (\text{A4})$$

Where A, B, C, D are given in Eq. (3).

Appendix B: Calculation with MPS and coherent state as inputs

The final state of the system at the output of the interferometer can be written as

$$|\psi'\rangle_{out} = N_j (A|K'\rangle + B|L'\rangle + C|M'\rangle + D|N'\rangle)_{a,b,E_a,E_b}, \quad (\text{B1})$$

with, N_j is given in Eq. (4), A, B, C, D are given in Eq. (3) and $|K'\rangle, |L'\rangle, |M'\rangle$ and $|N'\rangle$ are given as

$$\begin{aligned} |K'\rangle &= |k'_1, k'_2, k'_3, k'_4\rangle, \\ |L'\rangle &= |l'_1, l'_2, l'_3, l'_4\rangle, \\ |M'\rangle &= |m'_1, m'_2, m'_3, m'_4\rangle, \\ |N'\rangle &= |n'_1, n'_2, n'_3, n'_4\rangle. \end{aligned} \quad (\text{B2})$$

Where,

$$\begin{aligned} k'_1 &= k_1 + \varsigma', \quad k'_2 = k_2 + \vartheta', \quad k'_3 = k_3 + \bar{r}', \quad k'_4 = k_4 + \bar{r}\zeta, \\ l'_1 &= l_1 + \varsigma', \quad l'_2 = l_2 + \vartheta', \quad l'_3 = l_3 + \bar{r}', \quad l'_4 = l_4 + \bar{r}\zeta, \\ m'_1 &= m_1 + \varsigma', \quad m'_2 = m_2 + \vartheta', \quad m'_3 = m_3 + \bar{r}', \\ m'_4 &= m_4 + \bar{r}\zeta, \quad n'_1 = n_1 + \varsigma', \quad n'_2 = n_2 + \vartheta', \\ n'_3 &= n_3 + \bar{r}', \quad n'_4 = n_4 + \bar{r}\zeta, \quad \vartheta' = -it\zeta e^{\frac{i\phi}{2}} \sin\left(\frac{\phi}{2}\right), \\ \varsigma' &= it\zeta e^{\frac{i\phi}{2}} \cos\left(\frac{\phi}{2}\right), \quad \bar{r} = ir/\sqrt{2}, \quad \bar{r}' = -re^{i\phi}\zeta/\sqrt{2}. \end{aligned} \quad (\text{B3})$$

The density operator ($\hat{\rho}'_{out}$) is written as

$$\begin{aligned}
 \hat{\rho}_{out} = & |\psi\rangle_{out} \langle \psi| = |N_j|^2 (|A|^2 |K'\rangle \langle K'| \\
 & + |B|^2 |L'\rangle \langle L'| + |C|^2 |M'\rangle \langle M'| + |D|^2 |N'\rangle \langle N'| \\
 & + AB^* |K'\rangle \langle L'| + BA^* |L'\rangle \langle K'| + AC^* |K'\rangle \langle M'| \\
 & + CA^* |M'\rangle \langle K'| + AD^* |K'\rangle \langle N'| + DA^* |N'\rangle \langle K'| \\
 & + BC^* |L'\rangle \langle M'| + CB^* |M'\rangle \langle L'| + BD^* |L'\rangle \langle N'| \\
 & + DB^* |N'\rangle \langle L'| + CD^* |M'\rangle \langle N'| + DC^* |N'\rangle \langle M'|).
 \end{aligned} \quad (B4)$$

Where A, B, C, D are given in Eq. (3).

Now, from Eq. (38), the probability of getting m photon at port b , i.e., the coincidence rate by Eq. (19) can be written as

$$\begin{aligned}
 P(n) = & |N_j|^2 \left(|A|^2 e^{-|k'_1|^2} \frac{(|k'_1|^2)^n}{n!} + |B|^2 e^{-|l'_1|^2} \frac{(|l'_1|^2)^n}{n!} + |C|^2 e^{-|m'_1|^2} \frac{(|m'_1|^2)^n}{n!} + |D|^2 e^{-|n'_1|^2} \frac{(|n'_1|^2)^n}{n!} \right. \\
 & + e^{-|\alpha|^2} \left(AB^* e^{k'_2 l'_2 + k'_3 l'_3 + k'_4 l'_4} \frac{(k'_1 l'_1)^n}{n!} + A^* B e^{k'_2 l'_2 + k'_3 l'_3 + k'_4 l'_4} \frac{(k'_1 l'_1)^n}{n!} + AC^* e^{k'_2 m'_2 + k'_3 m'_3 + k'_4 m'_4} \frac{(k'_1 m'_1)^n}{n!} \right. \\
 & + A^* C e^{k'_2 m'_2 + k'_3 m'_3 + k'_4 m'_4} \frac{(k'_1 m'_1)^n}{n!} + AD^* e^{k'_2 n'_2 + k'_3 n'_3 + k'_4 n'_4} \frac{(k'_1 n'_1)^n}{n!} + A^* D e^{k'_2 n'_2 + k'_3 n'_3 + k'_4 n'_4} \frac{(k'_1 n'_1)^n}{n!} \\
 & + BC^* e^{l'_2 m'_2 + l'_3 m'_3 + l'_4 m'_4} \frac{(l'_1 m'_1)^n}{n!} + B^* C e^{l'_2 m'_2 + l'_3 m'_3 + l'_4 m'_4} \frac{(l'_1 m'_1)^n}{n!} + BD^* e^{l'_2 n'_2 + l'_3 n'_3 + l'_4 n'_4} \frac{(l'_1 n'_1)^n}{n!} \\
 & \left. \left. + B^* D e^{l'_2 n'_2 + l'_3 n'_3 + l'_4 n'_4} \frac{(l'_1 n'_1)^n}{n!} + CD^* e^{m'_2 n'_2 + m'_3 n'_3 + m'_4 n'_4} \frac{(m'_1 n'_1)^n}{n!} + C^* D e^{m'_2 n'_2 + m'_3 n'_3 + m'_4 n'_4} \frac{(m'_1 n'_1)^n}{n!} \right) \right) \quad (B5)
 \end{aligned}$$

The probability of getting an even and odd number of

photons, i.e., $P(\pm)$, form Eq. (B5) is written as

$$\begin{aligned}
 P(\pm) = & |N_j|^2 \left(|A|^2 \left(\frac{1 \pm e^{-2G-W}}{2} \right) + (|B|^2 + |D|^2) \left(\frac{1 \pm e^{-2G}}{2} \right) + |C|^2 \left(\frac{1 \pm e^{-2G+W}}{2} \right) \right. \\
 & + e^{-(|\alpha|^2 + |\zeta|^2)} \left((|A||B| + |A||D|) \left(e^{|\zeta|^2} \cos(q+p) \pm e^{S_1} \cos(q-p-W) \right) \right. \\
 & + (|B||C| + |C||D|) \left(e^{|\zeta|^2} \cos(q+p) \pm e^{S_2} \cos(q-p+W) \right) + |B||D| \left(e^{|\alpha|^2 - |\zeta|^2} \cos(j\pi) \pm e^{S_1 - T_1} \cos(j\pi - 2W) \right) \\
 & \left. \left. + |A||C| \left(e^{|\alpha|^2 - |\zeta|^2} \pm e^{S_1 - T_1} \right) \cos(j\pi) \right) \right). \quad (B6)
 \end{aligned}$$

[1] M. K. Mishra, H. Prakash, and V. B. Jha, Ququats as superposition of coherent states and their application in quantum information processing, *International Journal of Quantum Information* **19**, 2150013 (2021).

[2] I. Kim, R. J. Martins, J. Jang, T. Badloe, S. Khadir, H.-Y. Jung, H. Kim, J. Kim, P. Genevet, and J. Rho, Nanophotonics for light detection and ranging technology, *Nature nanotechnology* **16**, 508 (2021).

[3] V. Giovannetti, S. Lloyd, and L. Maccone, Quantum metrology, *Physical review letters* **96**, 010401 (2006).

[4] J. Dowling, Quantum lidar-remote sensing at the ultimate limit, in *Louisiana State University Baton Rouge, AIR FORCE RE-SEARCH LABORATORY INFORMATION DIRECTORATE ROME RESEARCH SITE ROME* (Tech. Rep., 2009).

[5] K. K. Mishra, D. Yadav, G. Shukla, and D. K. Mishra, Non-classicalities exhibited by the superposition of Schrödinger's cat state with the vacuum of the optical

field, *Physica Scripta* **96**, 045102 (2021).

[6] A. N. Boto, P. Kok, D. S. Abrams, S. L. Braunstein, C. P. Williams, and J. P. Dowling, Quantum Interferometric Optical Lithography: Exploiting Entanglement to Beat the Diffraction Limit, *Phys. Rev. Lett.* **85**, 2733 (2000).

[7] C. W. Helstrom, *Quantum Detection and Estimation Theory* (Academic Press, San Diego, CA, 1976).

[8] S. Pirandola, B. R. Bardhan, T. Gehring, C. Weedbrook, and S. Lloyd, Advances in photonic quantum sensing, *Nature Photonics* **12**, 724 (2018).

[9] G. Shukla, K. M. Mishra, A. K. Pandey, T. Kumar, H. Pandey, and D. K. Mishra, Improvement in phase-sensitivity of a mach-zehnder interferometer with the superposition of schrödinger's cat-like state with vacuum state as an input under parity measurement, *Optical and Quantum Electronics* **55**, 460 (2023).

[10] B. T. Gard, C. You, D. K. Mishra, R. Singh, H. Lee, T. R. Corbitt, and J. P. Dowling, Nearly optimal measurement schemes in a noisy mach-zehnder interferometer with coherent and squeezed vacuum, *EPJ Quantum Technology* **4**, 1 (2017).

[11] G. Shukla, K. K. Mishra, D. Yadav, R. K. Pandey, and D. K. Mishra, Quantum-enhanced super-sensitivity of a Mach-Zehnder interferometer with superposition of Schrödinger's cat-like state and Fock state as inputs using a two-channel detection, *J. Opt. Soc. Am. B* **39**, 59 (2022).

[12] J. P. Dowling, Quantum optical metrology – the low-down on high-N00N states, *Contemporary Physics* **49**, 125 (2008).

[13] M. Born and E. Wolf, *Principles of optics: electromagnetic theory of propagation, interference and diffraction of light* (Elsevier, 2013).

[14] Y. Gao, P. M. Anisimov, C. F. Wildfeuer, J. Luine, H. Lee, and J. P. Dowling, Super-resolution at the shot-noise limit with coherent states and photon-number-resolving detectors, *J. Opt. Soc. Am. B* **27**, A170 (2010).

[15] M. W. Mitchell, J. S. Lundeen, and A. M. Steinberg, Super-resolving phase measurements with a multiphoton entangled state, *Nature* **429**, 161 (2004).

[16] J. G. Rarity, P. R. Tapster, E. Jakeman, T. Larchuk, R. A. Campos, M. C. Teich, and B. E. A. Saleh, Two-photon interference in a mach-zehnder interferometer, *Phys. Rev. Lett.* **65**, 1348 (1990).

[17] E. Distant, M. Ježek, and U. L. Andersen, Deterministic superresolution with coherent states at the shot noise limit, *Phys. Rev. Lett.* **111**, 033603 (2013).

[18] K. J. Resch, K. L. Pregnell, R. Prevedel, A. Gilchrist, G. J. Pryde, J. L. O'Brien, and A. G. White, Time-Reversal and Super-Resolving Phase Measurements, *Phys. Rev. Lett.* **98**, 223601 (2007).

[19] C. M. Caves, Quantum-mechanical noise in an interferometer, *Phys. Rev. D* **23**, 1693 (1981).

[20] G. Shukla, D. Salykina, G. Frascella, D. K. Mishra, M. V. Chekhova, and F. Y. Khalili, Broadening the high sensitivity range of squeezing-assisted interferometers by means of two-channel detection, *Opt. Express* **29**, 95 (2021).

[21] M. Xiao, L.-A. Wu, and H. J. Kimble, Precision measurement beyond the shot-noise limit, *Physical review letters* **59**, 278 (1987).

[22] J. P. Dowling, Quantum optical metrology—the low-down on high-n00n states, *Contemporary physics* **49**, 125 (2008).

[23] R. Demkowicz-Dobrzański, M. Jarzyna, and J. Kołodyński, Quantum limits in optical interferometry, *Progress in Optics* **60**, 345 (2015).

[24] A. N. Boto, P. Kok, D. S. Abrams, S. L. Braunstein, C. P. Williams, and J. P. Dowling, Quantum interferometric optical lithography: exploiting entanglement to beat the diffraction limit, *Physical Review Letters* **85**, 2733 (2000).

[25] P. Kok, H. Lee, and J. P. Dowling, Creation of large-photon-number path entanglement conditioned on photodetection, *Phys. Rev. A* **65**, 052104 (2002).

[26] V. Giovannetti, S. Lloyd, and L. Maccone, Advances in quantum metrology, *Nature photonics* **5**, 222 (2011).

[27] S. D. Huver, C. F. Wildfeuer, and J. P. Dowling, Entangled Fock states for robust quantum optical metrology, imaging, and sensing, *Phys. Rev. A* **78**, 063828 (2008).

[28] M. A. Rubin and S. Kaushik, Loss-induced limits to phase measurement precision with maximally entangled states, *Phys. Rev. A* **75**, 053805 (2007).

[29] X. M. Feng, G. R. Jin, and W. Yang, Quantum interferometry with binary-outcome measurements in the presence of phase diffusion, *Phys. Rev. A* **90**, 013807 (2014).

[30] Q. Wang, L. Hao, H. Tang, Y. Zhang, C. Yang, X. Yang, L. Xu, and Y. Zhao, Super-resolving quantum LiDAR with even coherent states sources in the presence of loss and noise, *Physics Letters A* **380**, 3717 (2016).

[31] B. C. Sanders, Review of entangled coherent states, *Journal of Physics A: Mathematical and Theoretical* **45**, 244002 (2012).

[32] J.-L. Chen, D. Kaszlikowski, L. C. Kwek, C. H. Oh, and M. Żukowski, Entangled three-state systems violate local realism more strongly than qubits: An analytical proof, *Physical Review A* **64**, 052109 (2001).

[33] M. Fedorov, P. Volkov, J. M. Mikhailova, S. Straupe, and S. Kulik, Entanglement of biphoton states: qutrits and ququarts, *New Journal of Physics* **13**, 083004 (2011).

[34] R. Prakash, Use of entangled coherent states in quantum teleportation and entanglement diversion, in *The First International Workshop on Entangled Coherent States and Its Application to Quantum Information Science—Towards Macroscopic Quantum Communications* (2013) pp. 103–110.

[35] S. Mancini *et al.*, International journal of quantum information, *INTERNATIONAL JOURNAL OF QUANTUM INFORMATION* (2021).

[36] E. Wigner, On the quantum correction for thermodynamic equilibrium, *Physical review* **40**, 749 (1932).

[37] M. Hillery, R. F. O'Connell, M. O. Scully, and E. P. Wigner, Distribution functions in physics: Fundamentals, *Physics reports* **106**, 121 (1984).

[38] R. Loudon, *The Quantum Theory of Light* (OUP Oxford, 2000).

[39] G. S. Agarwal, *Quantum Optics* (Cambridge University Press, Cambridge, England, 2012).

[40] M. G. Paris, Quantum estimation for quantum technology, *International Journal of Quantum Information* **7**, 125 (2009).

[41] A. Royer, Wigner function as the expectation value of a parity operator, *Physical Review A* **15**, 449 (1977).

[42] K. E. Cahill and R. J. Glauber, Density operators and quasiprobability distributions, *Physical Review* **177**, 1882 (1969).

[43] C. C. Gerry, A. Benmoussa, and R. Campos, Parity mea-

surements, heisenberg-limited phase estimation, and beyond, *Journal of Modern Optics* **54**, 2177 (2007).

[44] J. J. . Bollinger, W. M. Itano, D. J. Wineland, and D. J. Heinzen, Optimal frequency measurements with maximally correlated states, *Phys. Rev. A* **54**, R4649 (1996).

[45] X. Feng, G. Jin, and W. Yang, Quantum interferometry with binary-outcome measurements in the presence of phase diffusion, *Physical Review A* **90**, 013807 (2014).

[46] L. Cohen, D. Istrati, L. Dovrat, and H. Eisenberg, Super-resolved phase measurements at the shot noise limit by parity measurement, *Optics express* **22**, 11945 (2014).

[47] L. Cohen, D. Istrati, L. Dovrat, and H. Eisenberg, Experimental super-resolved phase measurements with shot-noise sensitivity, arXiv preprint arXiv:1311.2721 (2013).

[48] Q. Wang, L. Hao, Y. Zhang, L. Xu, C. Yang, X. Yang, and Y. Zhao, Super-resolving quantum lidar: entangled coherent-state sources with binary-outcome photon counting measurement suffice to beat the shot-noise limit, *Optics express* **24**, 5045 (2016).

[49] W. Qiang, H. Lili, T. Hongxia, L. Xianli, M. Haiwei, H. Lianfu, and Z. Yuan, Effects of real environments on the performance of quantum lidar, *Infrared Laser Eng.* **47**, 29 (2018).